JGR Atmospheres

RESEARCH ARTICLE
10.1029/2019JD031413

Key Points:
- Winter Arctic clouds simulated by the polar version of the Weather Research and Forecasting model are compared with satellite retrievals
- The cloud amount and cloud top height of model simulations agree well with those of satellite retrievals
- The downward longwave radiation at the surface shows realistic temporal variations, but is sensitive to the cloud microphysics scheme choice

Supporting Information:
- Supporting Information S1

Correspondence to:
S.-Y. Jun,
syjun@kopri.re.kr

Citation:
Cho, H., Jun, S.-Y., Ho, C.-H., & McFarquhar, G. (2020). Simulations of winter Arctic clouds and associated radiation fluxes using different cloud microphysics schemes in the Polar WRF: Comparisons with CloudSat, CALIPSO, and CERES. *Journal of Geophysical Research: Atmospheres*, *125*, e2019JD031413. https://doi.org/10.1029/2019JD031413

Received 25 JUL 2019
Accepted 6 JAN 2020
Accepted article online 8 JAN 2020

Simulations of Winter Arctic Clouds and Associated Radiation Fluxes Using Different Cloud Microphysics Schemes in the Polar WRF: Comparisons With CloudSat, CALIPSO, and CERES

Heeje Cho[1,2], Sang-Yoon Jun[2], Chang-Hoi Ho[1,3], and Greg McFarquhar[4,5]

[1]Computational Science and Technology, Seoul National University, Seoul, South Korea, [2]Korea Polar Research Institute, Incheon, South Korea, [3]School of Earth and Environmental Sciences, Seoul National University, Seoul, South Korea, [4]Cooperative Institute for Mesoscale Meteorological Studies, University of Oklahoma, Norman, OK, USA, [5]School of Meteorology, University of Oklahoma, Norman, OK, USA

Abstract Arctic cloud simulations of the polar-optimized version of the Weather Research and Forecasting model (Polar WRF) were compared with retrievals using the CloudSat and Cloud-Aerosol Lidar and Infrared Pathfinder Satellite Observation measurements. For the period from 1 December 2015 to 31 January 2016, a series of 24- to 48-hr simulations initialized daily at 00 UTC were examined. In particular, two cloud microphysics schemes, the Morrison double moment and the WRF single-moment 6-class (WSM6), were tested. The modeled cloud top heights had a correlation coefficient (r) of 0.69–0.72 with those from satellite retrievals, and a mean bias of less than 400 m. For the mean ice water content profile and mixed-phase cloud occurrence, the Morrison scheme's clouds were in better agreement with satellite retrievals than the WSM6. However, the use of the Morrison scheme resulted in underestimates of outgoing longwave radiation by -11.7 W m^{-2} compared to satellite observations. The bias was reduced to -0.4 W m^{-2} with the WSM6 which produced a stronger precipitation rate (by 10%) resulting in a drier and less-cloudy atmosphere. This also leads to the 7-W m^{-2} mean difference in the surface downward longwave radiation (DLR) between the schemes, which is large enough to explain the spread of the Arctic DLR in the current climate models. However, as the temporal variation in DLR showed good agreement with ground observations (r: 0.68–0.92), it is concluded that the Polar WRF can be useful for studying cloud effects on the winter Arctic surface climate.

Plain Language Summary Clouds are important for the Arctic climate, but simulating such clouds with numerical models is still challenging. The accuracy of model clouds has not been sufficiently examined due to the harsh Arctic environment obstructing cloud observations, especially during Arctic winters experiencing polar nights. This study compares the Arctic winter clouds simulated by a weather forecast model to cloud observations from active (lidar and radar) satellite instruments. The model successfully produced cloud patterns similar to the satellite observations. However, the choice of the cloud physics module in the model can modify the amount of cloud water significantly enough to affect the simulated surface climate.

1. Introduction

Clouds are an essential element in the Earth's heat and water budget. Clouds can significantly alter the Earth's radiation both at the top of atmosphere (TOA) and at the surface because the clouds' shortwave reflectivity and thermal emissivity are much higher than those of the surrounding atmosphere (Chou et al., 1998; Harrison et al., 1990; Liou, 2002). In addition, the generation, growth, and precipitation processes of clouds constitute the source and sink of atmospheric water vapor that is a strong greenhouse gas. The latent heat released during cloud processes, in balance with the radiative fluxes, plays a central role in shaping the vertical structure of the atmosphere on a climatological basis. Thus, the way that clouds are represented in numerical models should affect the simulation, prediction, and understanding of the Earth's climate (Cess et al., 1996; Colman, 2003; Soden & Held, 2006; Webb et al., 2006).

Recent Arctic observations have revealed large cloud amounts in the lower troposphere throughout the year (Cesana et al., 2012). This is important because the thermal forcing at the surface is more influenced by low-

level clouds than by high-level clouds (Kay et al., 2016). The surface downward longwave radiation (DLR) is known to have a large influence on the Arctic surface climate. The influence is enough to account for half of the winter-mean sea-ice variations that are heavily dependent on the vertical structure of the clouds (Park et al., 2015). On the other hand, the cloud's influence on the sea ice can feedback to the cloud itself because the horizontal extent of the sea ice determines the potential amount of surface evaporation from the open ocean that regulates the amount of Arctic cloud water. This two-way interaction between the clouds and the sea ice constitutes a feedback process (Klaus et al., 2016). Understanding how this feedback operates is required for a better understanding of the Arctic weather and climate (Curry et al., 1996; Goosse et al., 2018; Overland et al., 2016).

Recently, the winter season has attracted more attention from Arctic researchers due to the accelerated wintertime surface warming since the late 1990s along with the decline of sea-ice concentrations especially over the Atlantic sector of the Arctic Ocean (Comiso, 2006; Francis & Hunter, 2007). Numerous studies have shown that the Arctic sea-ice concentration over the Barents Sea has potential predictability for the near-surface temperatures over the Eurasian continent during the winter season (Kim et al., 2014; Kug et al., 2015). Given the large influence of clouds on the underlying surface radiative budget (Graversen et al., 2008), the characteristics of Arctic winter clouds and their recent changes (Jun et al., 2016; Liu et al., 2007) should be examined in detail. However, relatively few winter Arctic cloud studies have been reported compared to other seasons. This is due to the difficulty in obtaining wintertime Arctic observations owing to the harsh weather conditions, lack of visibility, and the sea ice that covers most of the Arctic Ocean (Arctic Climate Impact Assessment, 2005; Karlsson & Svensson, 2011). Even for a satellite-borne instrument like the Moderate Resolution Imaging Spectroradiometer (MODIS), cloud detection can be less accurate (Chan & Comiso, 2013) and the retrievals of cloud optical properties (such as optical thickness or droplet effective radius) based on solar techniques are impossible in regions that experience polar night.

Model-based Arctic research has been hampered by the scarcity of observations (Kay et al., 2016). In the polar regions, climate model simulations have larger across-model spread than other regions, and the disagreement is largest during the winter season (Chernokulsky & Mokhov, 2012; Intergovernmental Panel on Climate Change, 2013; Karlsson & Svensson, 2011, 2013). However, the uncertainty of the global climate model in simulating the Arctic winter can be reduced by utilizing a regional model. Regional models are better for representations of the surface climate, as well as the cloud characteristics, due to additional constraints given by prescribing lateral boundary conditions. Further, as they usually allow for a higher spatial resolution, a more accurate simulation might be expected (Jung et al., 2006; Pope & Stratton, 2002). The polar-optimized version of the Weather Research and Forecasting (Polar WRF) model has been used for studies on clouds in polar regions to reveal the cloud's role in the Arctic climate and its interaction with the recent sea-ice changes (Barton & Veron, 2012). The accuracy of cloud properties simulated by the Polar WRF has increased due to the growing coverage of Arctic ground stations and a number of field observation campaigns providing better data for initializing models and process-based understanding required for parameterization development. In addition, newly developed and improved cloud microphysics schemes made a substantial contribution to the improved simulation (Listowski & Lachlan-Cope, 2017). Still, winter season clouds have yet to be sufficiently examined in either observational or modeling studies.

Active instruments can provide invaluable Arctic cloud observations during the winter season because their observations are not restricted by solar light conditions. In addition, vertically resolved cloud structures can be obtained using these observations. This study utilizes cloud observations from two satellite-borne active instruments, namely, the Cloud Profiling Radar (CPR) onboard the CloudSat satellite (Stephens et al., 2002) and the Cloud-Aerosol Lidar with Orthogonal Polarization (CALIOP) onboard the Cloud-Aerosol Lidar and Infrared Pathfinder Satellite Observations (CALIPSO) satellite (Winker et al., 2009). Launched in 2006, these two instruments were placed into the Afternoon Constellation orbit, the so-called “A-train.” By comparing with the cloud observations from MODIS onboard the Aqua satellite that is also a member of the A-train, the benefits of cloud retrievals from the CPR and CALIOP (Chan & Comiso, 2011, 2013; Liu et al., 2012) in detecting wintertime low-level arctic clouds can be shown since MODIS has trouble distinguishing them from underlying sea ice (Chan & Comiso, 2013).

Because the radiative fluxes at the surface and the TOA are greatly influenced by cloud structure, their accuracy in a model requires successful cloud simulations. The radiative fluxes are also tightly linked to

air temperature and humidity profiles that directly affect the cloud processes in the model simulations. Accurate radiative fluxes in model simulations, therefore, require a realistic representation of clouds. Furthermore, as fluxes are directly observed by instruments from satellites or ground stations, and cloud properties are retrieved from such fluxes, the direct evaluation of radiative fluxes can be an invaluable comparison in addition to that of the cloud properties themselves. Clouds and the Earth's Radiant Energy System (CERES; Wielicki et al., 1996) is a satellite-borne instrument that provides a direct measure of the radiative fluxes at the TOA that can be compared with those from WRF simulations. At the surface, despite the difficulty of wintertime Arctic ground observations, radiative flux measurements at six ground sites are available from the Baseline Surface Radiation Network (BSRN) data set (Driemel et al., 2018).

The primary goal of the present study is to compare the Polar WRF simulation of a selected winter against observations, in order to assess the model performance regarding its simulation of winter Arctic clouds. This offers useful guidance for further winter Arctic modeling applications using the Polar WRF. In particular, a reference data set was created to correspond to the temporal and spatial scales of the model output to facilitate a proper evaluation of the mesoscale model. These observations provide the vertical structure of clouds that are particularly important for determining the cloud radiative effect during the winter season and longwave radiative fluxes at the surface and the TOA. Two cloud microphysics schemes that are widely used for polar region applications were tested in order to evaluate the cloud uncertainty due to the choice of the microphysics scheme.

2. Method

2.1. Model Simulation

The Polar WRF version 3.7.1 (Hines & Bromwich, 2017; Skamarock et al., 2008) applying a polar stereographic projection with the center at the North Pole was used with 30 vertical terrain-following sigma levels from the Earth's surface to 50 hPa. The vertical resolution is ~50 m near the surface, increasing to ~500 m at 3-km height, and to ~1 km near the tropopause. A domain of 300 × 300 grids with a 24-km resolution encompassed the area with latitudes higher than 56.5°N (Figure 1). The winter of 2015–2016 that was characterized by a strong Arctic storm season with an above-average number of organized snow storms (McCarthy et al., 2016) was simulated. As such, a variety of cloud features were obtained, not only ubiquitous low-level stratus near the surface but also Arctic storms that extended to the tropopause. During this period, the entry of a strong windstorm into the Arctic Ocean, known to trigger the abrupt shift of the Arctic Oscillation from a positive to a negative phase, occurred around early January 2016 (Kim et al., 2017). This, as a result, allows the evaluation of model performance under a wide variety of environmental conditions. Successive 48-hr simulations were performed beginning at 00 UTC every day between 1 December 2015 and 31 January 2016. The simulations were initialized and laterally updated using the National Center for Environmental Prediction (NCEP) Final Operational Global Analysis data (NCEP, 2000) and the NCEP Real-Time Global Sea Surface Temperature data (Thiébaux et al., 2003) every 6 hr. With a series of two-day simulations, we used hourly outputs except for the initial 24-hr spin-up segments for the analysis following Wilson et al. (2012) and Hines and Bromwich (2017). The domain average times series of precipitation, precipitable water, and radiative fluxes were examined to make sure that the 24-hr spin-up is long enough for the model to reach a stable state (not shown). In order to assess the importance of varying processes on the Arctic clouds, two cloud microphysics schemes that are widely used in Arctic applications, namely, the Morrison double moment scheme (Morrison et al., 2005) and the WRF single-moment 6-class (WSM6) scheme (Hong & Lim, 2006), were used in separate model simulations. The choice of other physics schemes in the WRF simulations were as follows: the Rapid Radiative Transfer Model for the longwave radiative transfer (Mlawer et al., 1997), Goddard shortwave scheme for the shortwave radiative transfer (Chou et al., 1998), Mellor–Yamada–Janjić scheme for the planetary boundary layer (Janjić, 1994), Unified Noah model for the land surfaces (Tewari et al., 2004), Grell–Devenyi ensemble scheme for the cumulus parameterizations (Grell & Dévényi, 2002), and the Eta similarity scheme for the surface layer (Janjić, 1994).

For clarity, the term “cloud” in the manuscript refers to the existence of any hydrometeor category; therefore, any quantity of cloud is a summed value of all categories including rain, ice, snow, and graupel particles. “Liquid” means liquid-phase cloud water without including the “rain” water. Similarly, “ice” means ice

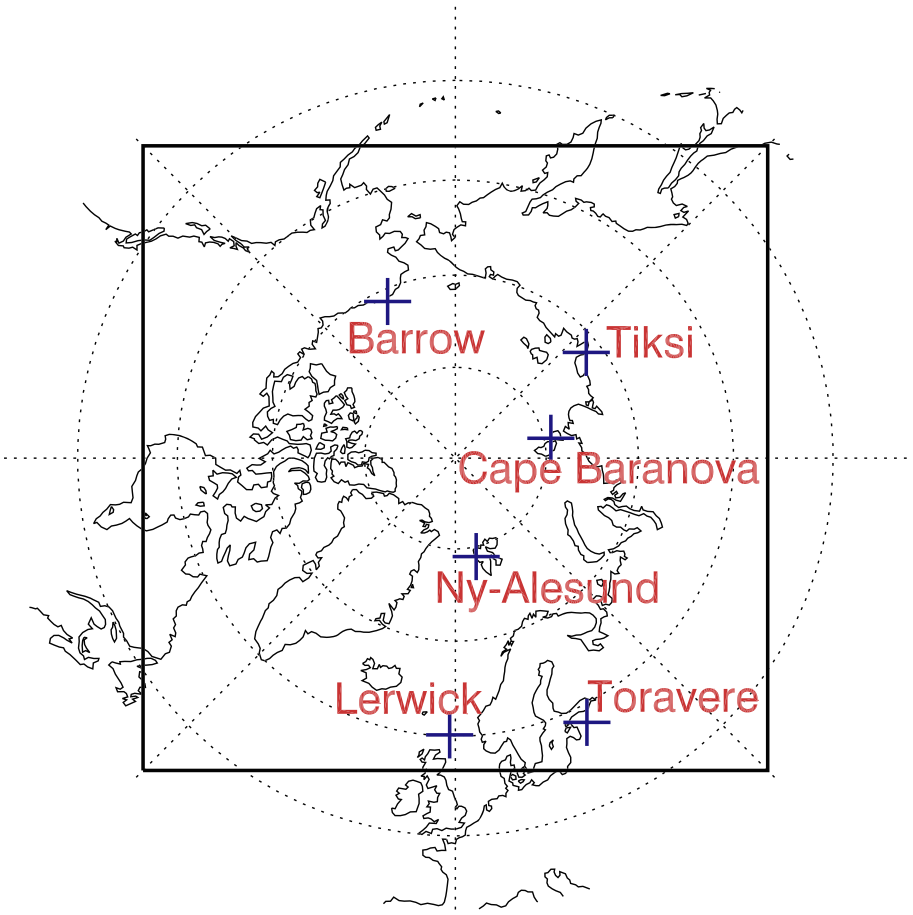

Figure 1. Model domain used for the Polar WRF simulations. The domain consisted of 300 × 300 grid points with a 24-km horizontal resolution. Crosses indicate the locations of the ground sites used for radiation observations.

cloud water so it does not include "snow" or "graupel" particles. The term "frozen" particle in the manuscript is used to refer to ice, snow, or graupel particles collectively.

2.2. Satellite Data

DARDAR (raDAR/liDAR) cloud products are derived from the combination of CloudSat radar and CALIPSO lidar observations (Delanoë & Hogan, 2008, 2010). This combination is more synergistic for observing winter Arctic clouds with small water contents and large low-level fractions, although the accuracy of the products has not been tested by comparison with independent cloud observations. As active instruments, both CPR and CALIOP are the best ways to retrieve cloud microphysical variables over regions that experience polar night. The optical thickness of Arctic clouds is expected to be less during the winter season than other seasons because the amount of cloud water is limited by the extremely cold air temperatures and reduced fetch from the frozen ocean surface. Thus, CALIOP's lidar observations can help detect clouds with small droplet sizes that are not well detected by the CPR's radar. On the other hand, low-level cloud observations from CALIOP can be blocked by thick clouds above due to the lidar signal attenuation. Thus, any information on these low-level clouds detected by the CPR is beneficial. This complementary retrieval is valuable considering that the vertically contiguous clouds that extend from the lower troposphere to the upper troposphere are frequent during wintertime in the Arctic regions (Oreopoulos et al., 2017). In this study, a three-dimensional cloud mask and ice water contents were used that are produced for the same horizontal (about 1 km) and vertical (60 m) resolutions with the CloudSat observations. These scales are much smaller than the resolution of the model simulations. Although the comparison might be affected by the discrepancy in

scale between the satellite observations and the model simulations, it can provide useful information for future Polar WRF applications with similar configurations. In addition, the sensitivity of clouds to model resolution is known to be mostly related to convection processes (e.g., Bryan & Morrison, 2012) which are less significant in the Arctic environment.

Observations from the CERES instrument onboard the Aqua satellite were also used. The single scanner footprint (SSF Aqua-FM3 edition 4A) product offers not only direct measurements of the TOA longwave flux but also estimates of the surface longwave flux produced using radiative transfer calculations. The surface flux is parameterized based on a priori information on cloud base heights and atmospheric profiles of air temperature, humidity, and ozone (Kratz et al., 2010). The mean bias and root-mean-square error of the CERES surface longwave flux to the ground observations was about −0.5 and 10.3 W m^{-2}, respectively (https://ceres.larc.nasa.gov/science_information.php?page=computed-fluxes). Note that the CERES footprints are 25 km in diameter near nadir.

The statistical comparisons with the model simulations were mostly performed using the level-2 observations from the satellites. Each observation point was assigned to the WRF grid that enclosed it. Because the grid size of the WRF simulation is larger than the footprint sizes of the satellite observations, a simple average of the satellite observations was compared to the value for the WRF grid that enclosed it. Further, from the hourly WRF outputs, the simulation that was nearest in time to the satellite observation was chosen. Thus, any element of the WRF-satellite-matched data sets was always within at least 12 km in space and 30 min in time. During the two-month period, 125,318 WRF grids were collocated with the DARDAR data set and 362,306 WRF grids were collocated with the CERES data set.

The satellite cloud properties are fundamentally different from model-simulated clouds because they are based on retrievals. To enable a more direct comparison between satellite-observed clouds and model-simulated clouds, the radar simulator (Haynes et al., 2007) and the lidar simulator (Chepfer et al., 2008) integrated into the Cloud Feedback Model Inter-comparison Project Observational Simulator Package (COSP; Bodas-Salcedo et al., 2011) version 1.4 were used. The simulators were applied to the Polar WRF output to mimic satellite-like radar or lidar signals so they could be directly compared to the CloudSat and CALIPSO observations, following the offline calculation approach by Diaz et al. (2015).

2.3. Surface Longwave Flux Observations

Direct measurements of the downward longwave radiative flux at the surface were also used to evaluate the model simulations. During the simulation period, six Arctic and high-latitudinal ground sites were available within the BSRN data set (see crosses in Figure 1), namely, Cape Baranova, Russia (79.27°N, 101.75°E); Ny-Ålesund, Norway (78.93°N, 11.93°E); Tiksi, Russia (71.59°N, 128.92°E); Barrow, USA (71.32°N, 156.61°W); Lerwick, United Kingdom (60.14°N, 1.18°W); and Tõravere, Estonia (58.25°N, 26.46°E). All stations are located near the coast except for the Tõravere station that is about 100 km away from the Baltic Sea. However, as the Arctic Ocean in front of Cape Baranova, Tiksi, and Barrow were covered by sea ice during the entire simulation period, different meteorological conditions are thus considered in the analysis. The use of observations from the stations at coastal regions might influence the model evaluation because a strong gradient effect due to land-sea contrast can occur on scales smaller than the grid size. However, the discontinuity in the cloud water path from reanalysis data is small across coastlines near ice-covered coastal seas because the gradients between land surface and ice-covered ocean are much weaker than those between land surface and open ocean or those between ice-covered ocean and open ocean. Note that the Cape Baranova observations have only been available since 1 January 2016.

3. Results

3.1. Macrophysical Properties

The macrophysical properties of clouds in the Polar WRF simulations are compared to those of the DARDAR cloud mask in Table 1. The values were obtained for all areas under the satellite paths including cloud-free areas. Note that the existence of a modeled cloud is defined when the total mixing ratio of all cloud hydrometeors exceeds 10^{-9} kg kg^{-1}.In the collocation data set that combines the Polar WRF simulation and the DARDAR cloud mask (Table 1), the top height of the cloud was higher by 290 m on average when the Morrison double-moment scheme was used to represent the cloud microphysics. This is smaller than the

Table 1
Mean Heights of Cloud Top in the DARDAR (raDAR/liDAR) Cloud Data (Combined Cloud Retrievals Using CloudSat and CALIPSO) and in the Polar WRF Simulations

	DARDAR	P-WRF (Morrison)	P-WRF (WSM6)
Cloud top height (correlation with DARDAR)	5590 m (-)	5880 m (0.72)	5230 m (0.69)

Note. The values in parentheses denote the correlation coefficients between the DARDAR cloud heights and the modeled cloud heights. The Morrison scheme and the WSM6 scheme were used for the cloud microphysics in the simulations.

vertical resolution of the model simulations which is larger than 500 m above a 3-km height from the surface. The mean bias was also small using the WSM6 scheme as the cloud top height was lower than the DARDAR data set by 360 m. The correlation coefficient between the DARDAR's cloud top height and the Polar WRF cloud top height was 0.72 with the Morrison scheme and 0.69 with the WSM6 scheme assuring that the model processes were correctly producing the cloud top heights. When the CALIPSO cloud mask was used instead of the DARDAR data set, the correlation coefficients were similar but the modeled cloud top was lower than the CALIPSO retrievals by 90 and 720 m for the Morrison scheme and the WSM6 scheme, respectively (Table S1). Van Weverberg et al. (2013) found that, with the WSM6 scheme, the fall speed of ice particles in the upper troposphere is faster than with the Morrison scheme, which likely contributes to the higher cloud top with the Morrison scheme.

Cloud amounts were defined differently in Figures 2a and 2b. In Figure 2a, "cloud occurrence" is defined as 0 or 1 when a WRF grid is cloud-free or cloudy, respectively. For DARDAR, it is 0 if there is no cloud in the satellite observations within the collocated WRF grid; otherwise, it is 1. In Figure 2b, the "cloud fraction" for the Polar WRF simulation is the model output variable with the same name diagnosed by the WRF's radiation code. For DARDAR, it is the ratio of the number of cloudy observations to the number of total observations within the collocated WRF grid. The geometric height given in the DARDAR for the vertical coordinate was converted into the vertical coordinate of the WRF simulation for the comparisons. At the bottom level, clouds were found at about 60 to 65% of the total collocated grid points in the model simulations (Figure 2a), similar to the 65% coverage reported by Karlsson and Svensson (2013) and Kay et al. (2016). Figure 2a reveals that clouds are very likely to exist at the model's bottom level, consistent with the appearance of many

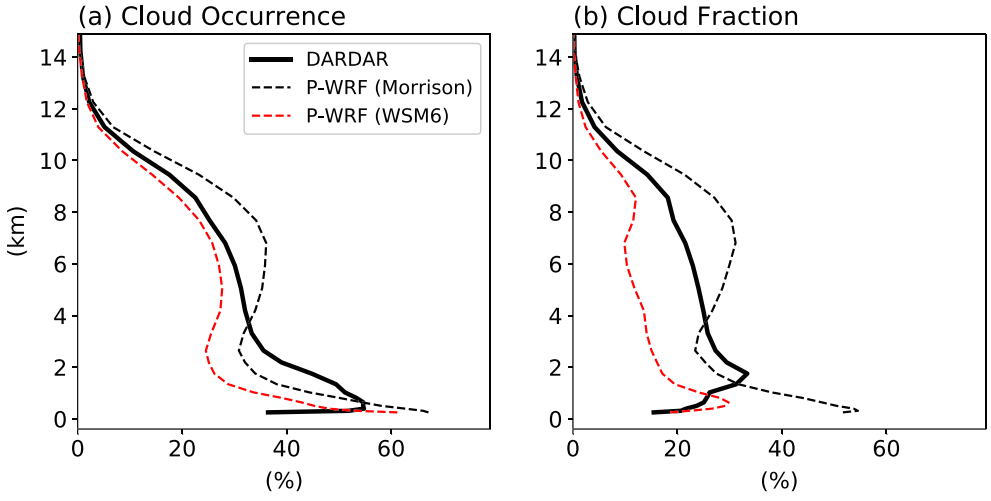

Figure 2. Mean vertical structures of the cloud amounts in the DARDAR cloud data (solid) and the collocated Polar-WRF simulations (dashed). Different definitions of the cloud amount were used. (a) "Cloud occurrence" is defined as 1 if cloud existed in a WRF grid and (b) "cloud fraction" is defined as the ratio of cloudy pixels within a collocated WRF grid for the DARDAR and the value with the same name for the model output. Black dashed lines represent the Polar WRF simulations with the Morrison scheme and red dashed lines for the WSM6 scheme.

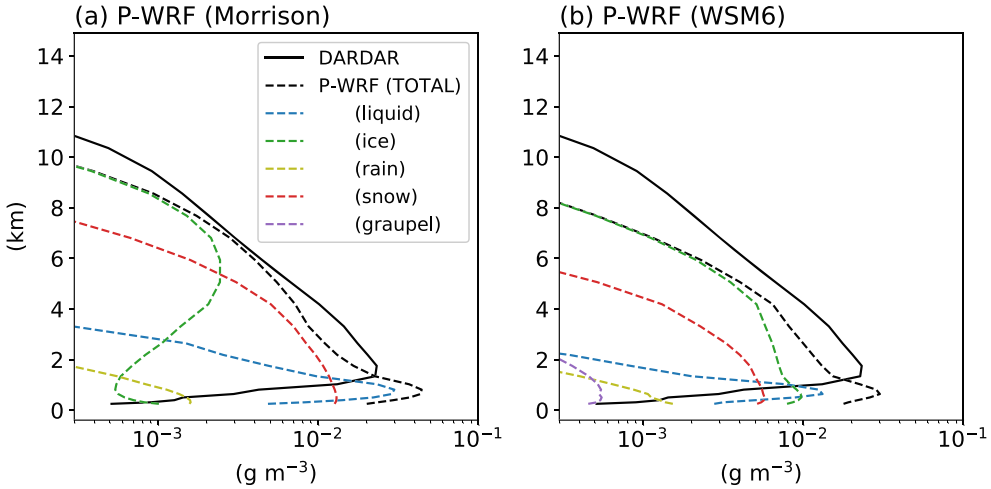

Figure 3. Mean vertical structures of the ice water content in the DARDAR cloud data (solid) and the cloud water content for each hydrometeor in the collocated Polar-WRF simulations (dashed). The blue, green, yellow, red, and purple dashed lines are for the liquid, ice, rain, snow, and graupel particles, respectively. The black dashed lines are for the total cloud water contents. (a) The Morrison scheme and (b) the WSM6 scheme were used for the cloud microphysics in the Polar-WRF simulations.

low-level boundary clouds in the Arctic. Therefore, temporal or spatial variations in the base height of modeled clouds can be too small to quantify. The discrepancy at levels below 2 km between the satellite retrievals and the model is likely due to the different vertical coordinate between the satellite data and the model simulations. In addition, there are possibilities that small cloud particles in low-level clouds cannot be detected by the CloudSat radar, especially when they are located below thick clouds with large particle sizes. Further, the uncertainty of CloudSat radar observations tends to be larger below 1-km height owing to signal reflections from the surface. Note that the cloud occurrence, by definition, may increase with grid size, which is the 24-km grid resolution of WRF in this case, not the footprint resolution of the satellite observations. With the WSM6 scheme, the mean cloud amount is smaller than that of the Morrison scheme at every level, for both measures, showing small cloud fractions (Figure 2b) less than 20% throughout the troposphere above 1.5-km height and even near the surface.

3.2. Optical Properties

Figure 3 shows the vertical structures of the mean cloud water content in the DARDAR cloud data set (solid line) and the Polar WRF simulations (dashed line). The cloud water contents of each hydrometeor in the Polar WRF simulations are illustrated with colored dashed lines. The entire collocated data set including the data over cloud-free areas was used to quantify the mean structure. Note that only ice-phase cloud particles are considered in the DARDAR retrievals (Delanoë & Hogan, 2008, 2010). The magnitude of the total cloud water contents in the Polar WRF simulation shows good agreement with the satellite observations, especially when the Morrison scheme was used (black dashed line in Figure 3a). However, the magnitude was slightly smaller above 2 km and larger below 2 km. The major hydrometeor categories in the Polar WRF simulations were ice, snow, and liquid. Despite the cold air temperature, it was noted that liquid-phase clouds were the most dominant type beneath about 1.5 km. Supercooled- or mixed-phase clouds are frequently found in the scene-type retrievals in the DARDAR data sets, as many modeling and observational studies have noted the existence of liquid-phase Arctic clouds in the form of a mixed-phase or supercooled liquid water (McFarquhar et al., 2007; Morrison et al., 2003; Pinto, 1998; Shupe et al., 2006). The larger cloud water contents in the Polar WRF simulations than in the satellite retrievals below 2 km (black solid lines in Figures 3a and 3b) may be partly because only the ice-phase clouds are considered in the DARDAR retrieval algorithm. While both the ice and the snow are frozen hydrometeors, snow is the dominant category when the Morrison scheme is used (red dashed line in Figure 3a) and the ice cloud is dominant when the WSM6 scheme is used (green dashed line in Figure 3b).

The overall characteristics of the cloud water contents for each hydrometeor can be more closely revealed by examining a representative case. Figures 4 and 5 show the vertical structure of cloud water contents along

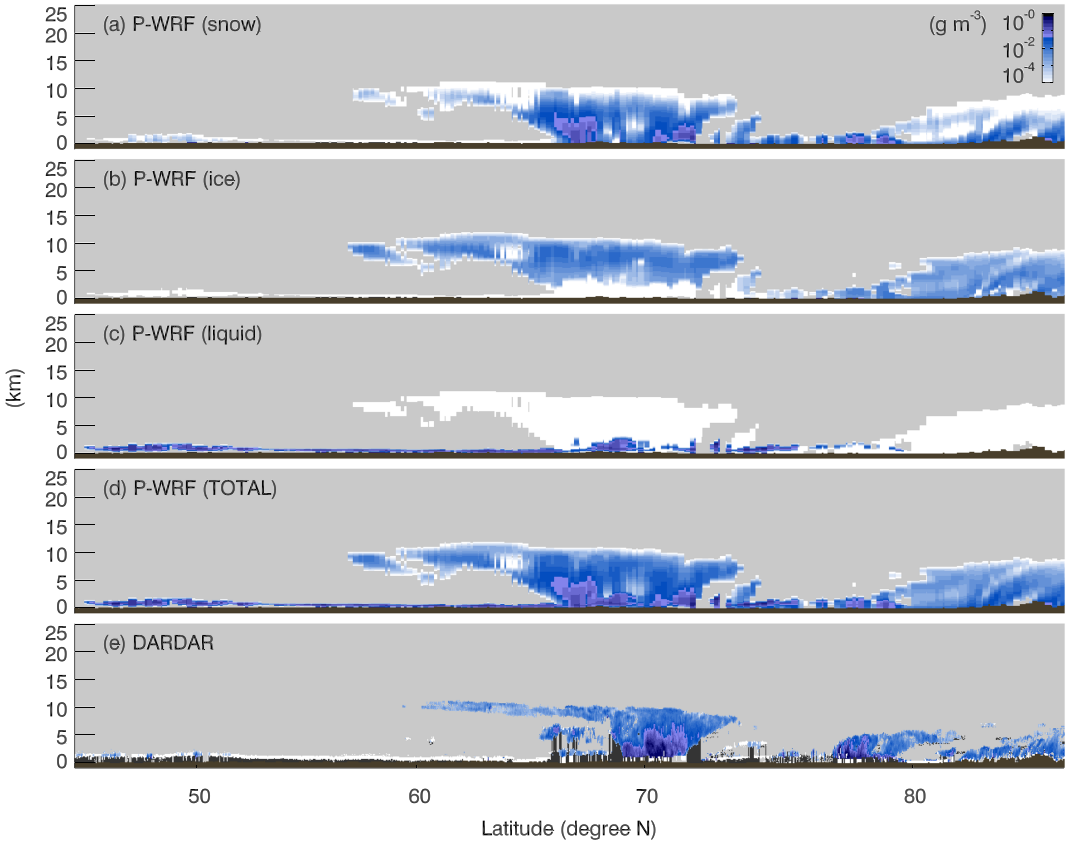

Figure 4. Cloud water content of (a) snow, (b) ice, (c) liquid, and for (d) all hydrometeors from the Polar WRF simulation with the Morrison scheme, and (e) the ice water content from the DARDAR cloud data along an A-train track around 10 UTC, 25 December 2015. The color scale is the $\log_{10}$ of the cloud water content.

the satellite track around 10 UTC, 25 December 2015, compared to the collocated Polar WRF simulations with the Morrison scheme (Figure 4) and the WSM6 scheme (Figure 5). The top three subfigures show the most dominant hydrometeors: snow, ice, and liquid (Figures 4a–4c and 5a–5c). The fourth is the summed cloud water content in the Polar WRF simulation (Figures 4d and 5d) and the last one is the ice water content retrievals from the DARDAR cloud data set (Figures 4e and 5e). The white-to-blue color gradient shows the cloud water contents where clouds are detected. Gray and dark brown colors correspond to cloud-free and surface areas, respectively. Along the entire track, near-surface stratus clouds were found for both the DARDAR observations and the WRF simulation. In the DARDAR observations, the ice water contents of the stratus clouds were very small (white areas) up to the south of around 65°N, as shown in the mean vertical profile in Figure 3 (black lines below 1 km). This was also true for the WRF simulation showing that the clouds over that area mostly consisted of liquid-phase water (Figures 4c and 5c). In the vertically extended cloud around 70°N, near-surface level clouds were in liquid phase (Figures 4c and 5c). Above that level, the two cloud microphysics schemes resulted in different categorizations of frozen particles. Consistent with the mean vertical structures shown in Figure 3, the snow category was most dominant between 1 and 5 km with the Morrison scheme (Figure 4b), whereas the ice category was most dominant at all levels above 1 km with the WSM6 scheme (Figures 5a and 5b). The deep clouds around 85°N showed a similar structure but without the near-surface liquid-phase layers. In the low-level clouds around 75°N, the Morrison scheme simulated larger liquid water contents at the tops of the clouds than below (Figure 4c). This mixed- or supercooled-phase cloud layer on top of the ice-phase cloud is an observed feature of Arctic clouds (e.g., McFarquhar et al., 2007) that is also found in the cloud phase retrievals in the DARDAR data set (figure not shown). Unlike with the Morrison scheme, the water content of the ice cloud with the WSM6 scheme is larger than that of snow in most of the

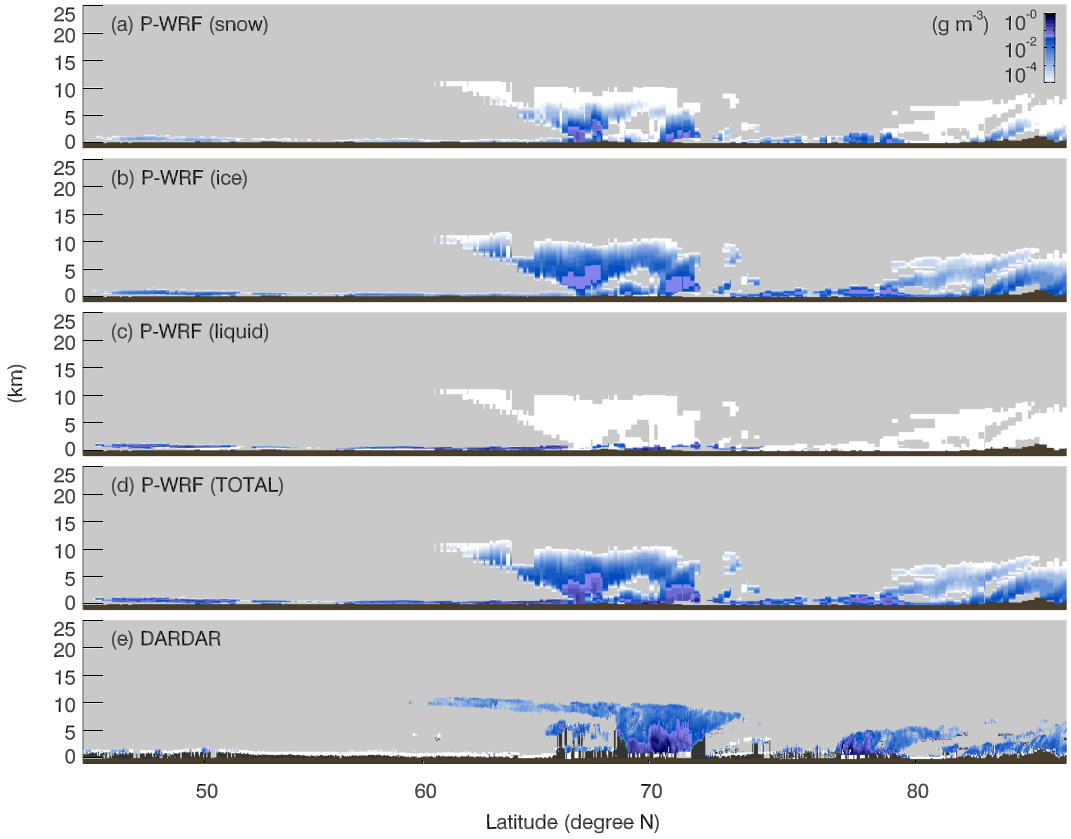

Figure 5. Same as Figure 4 but for the WSM6.

clouds along the satellite track (Figures 5a and 5b). Liquid-phase water in the WSM6 scheme (Figure 5c) is not as dominant as with the Morrison scheme in the near-surface stratus. The liquid-phase cloud layer on top of the ice-phase cloud at around 75°N was not simulated with the WSM6 scheme. The high-level ice clouds at a 10-km altitude around 60°N have large horizontal extensions. These cover larger areas with the Morrison scheme (Figure 4d) than the DARDAR cloud retrievals (Figure 4e) but are smaller with the WSM6 scheme (Figure 5d), which is also seen in the mean cloud amount at the level (Figures 2a and 2b). This difference in high cloud coverage may contribute to the differences in the cloud top height among them. Morrison has the highest, followed by DARDAR, and WSM6 was the lowest (Table 1).

Information on the particle phase of clouds is illustrated in Figure 6. As the DARDAR cloud data set assigns a cloud at each level as one of "ice," "ice + supercooled," "liquid warm," and "supercooled" cloud categories, the number of levels for each category was summed. The "MIXED" in the figure means the number of observation points of the ice + supercooled category. "LIQUID" means the total number of observation points of the liquid warm and supercooled categories (Figure 6a). For the Polar WRF simulations (Figures 6b and 6c), a WRF grid at each level is counted as LIQUID if it contains only liquid or rain particles, and as "ICE" if it has only frozen particles. MIXED means it contains both liquid and frozen cloud phases. Considering the vertical resolution of the simulations, the counts of WRF points are scaled to correspond to the DARDAR height resolution. Using the air temperature compiled in the DARDAR data set and that from the WRF simulations, the data were binned into air temperature intervals of 2 °C. In the DARDAR cloud retrievals, LIQUID or MIXED phase clouds (red and black lines in Figure 6a) were frequently detected and they account for about 40% of cloud observations at –20 °C. Arctic liquid-phase clouds are known to exist at temperatures greater than –40 °C, mostly below 3-km altitude (Shupe, 2011). The Morrison scheme (Figure 6b) simulated more liquid-phase clouds than the WSM6 scheme (Figure 6c) which is consistent with the mean cloud water content profile of each hydrometeor in Figure 3. For the Morrison scheme, as the temperature

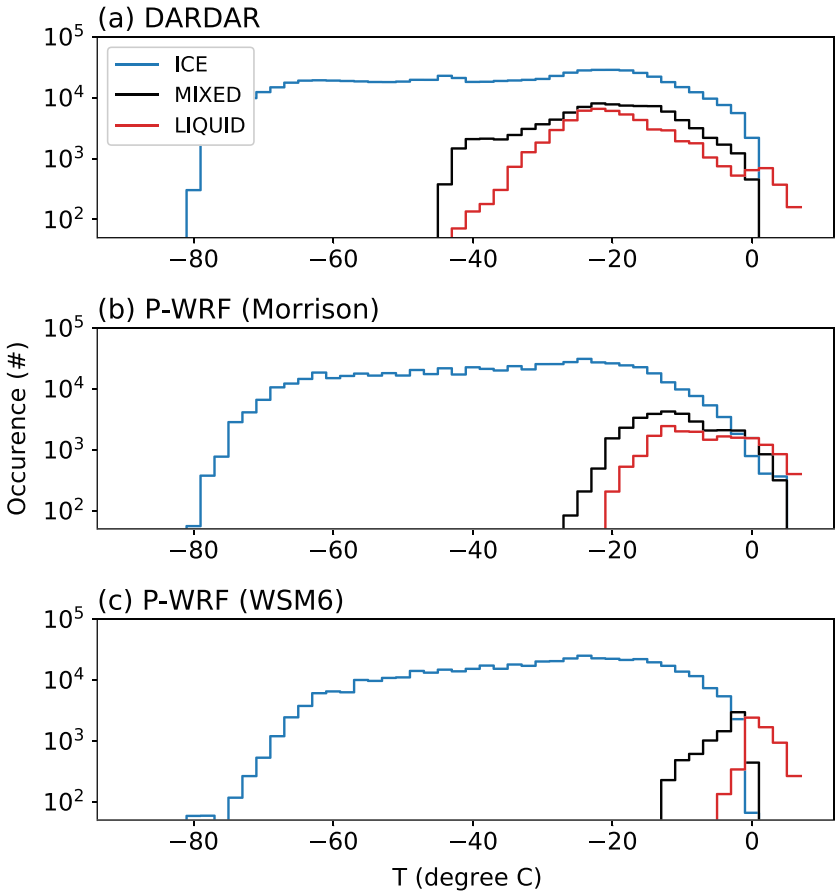

Figure 6. Number of points for each thermodynamic phase of clouds (liquid or rain phase = red, frozen phase = blue, and mixed phase = black). The data set is binned into the air temperature intervals of 2 °C. The numbers are counted for each WRF horizontal grids and are scaled to correspond to the 60-m height resolution of the DARDAR retrievals.

increases above −10 °C, the amount of mixed-phase clouds becomes significant, which is the case for the WSM6 scheme only for the warm atmosphere with a temperature above 0 °C. On the other hand, at temperatures below −20 °C, both the Morrison scheme and the WSM6 scheme produced a significantly smaller amount of liquid or rain particles than frozen particles.

Figure 7a shows the joint probability density function (PDF) of the CloudSat radar reflectivity and height. Figures 7b and 7c were obtained in the same manner, but for the simulated satellite-like radar reflectivity based on the Polar WRF model simulations using the Morrison scheme and the WSM6 scheme, respectively. The simulated radar signals were produced by the radar simulator compiled in the COSP package (Bodas-Salcedo et al., 2011). The observed CloudSat signal PDF (Figure 7a) shows a monotonic decrease in the reflectivity with altitude that implies that the clouds are thick near the surface and gradually get thinner above. In the COSP simulation results (Figures 7b and 7c), the occurrence of relatively strong radar signals at about 1 to 3 km also appears near the ground. A notable difference between CloudSat and the Polar WRF is that, below 5 km, strong reflectivity signals larger than 10 dBZ are frequently observed from CloudSat (Figure 7a), while the radar simulator results based on the Polar WRF simulations are clustered mostly at much weaker reflectivity (Figures 7b and 7c). When the satellite retrievals of cloud water contents were directly compared to the modeled cloud water contents (Figure 3), both the Morrison scheme and the WSM6 scheme seem to overestimate cloud water contents near the surface below about 1 km. However, the comparison via the radar simulator suggests that the small cloud water content retrievals from CloudSat near the surface could be unreliable; thus, Polar WRF's overestimation of cloud water contents below 1 km may not be large as Figure 3 showed.

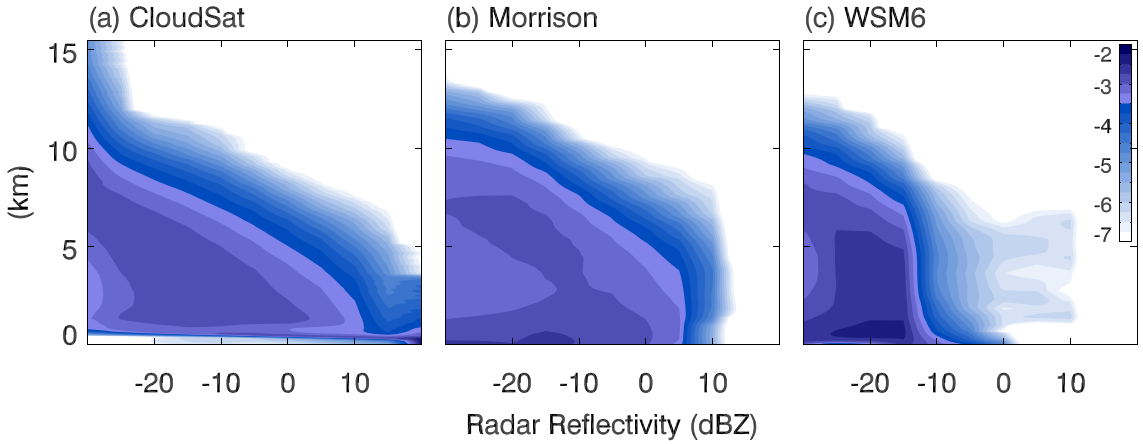

Figure 7. (a) Joint probability density function (PDF) of the CloudSat radar reflectivity and height. Polar WRF simulations with the (b) Morrison scheme and the (c) WSM6 scheme were converted to "satellite-like" radar reflectivity using the COSP package to obtain the joint PDF. The color scale is the $\log_{10}$ of the joint PDF.

The joint PDF of the lidar scattering ratio and height (Figure 8) highlights the discrepancy between the observation and the Polar WRF simulation. The lidar signal below 5 km is much more prominent in the lidar simulations based on the Polar WRF output than in the CALIPSO observations. For the CALIPSO observations (Figure 8a), the high occurrence cluster of the joint PDF is centered on the weaker signal at about 3- to 7-km height and the stronger signal at about 8- to 10-km height. This is not the case for the Polar WRF model simulations where the strong lidar scatterings were simulated near the surface level using both cloud microphysics schemes. The weak low-level signal in the CALIPSO observations occurs because the lidar signal is easily attenuated by the large droplets between the target and the sensor. Since it is highly probable that thick low-level cloud accompanies a thick middle- to high-level cloud (Oreopoulos et al., 2017), the occurrence of strong lidar scattering near the surface tends to be less frequent. In contrast, a stronger near-surface lidar scattering is expected from the Polar WRF simulations (Figures 8b and 8c). This could occur if the lidar simulator cannot represent attenuations that take place in the real CALIPSO observations. However, it seems likely that the modeled upper tropospheric clouds were not thick enough to block out lidar signals from lower tropospheric or near-surface levels. Similar characteristics were observed in the vertical structure of the modeled cloud water content (Figure 3) that is smaller than the satellite retrievals in the middle- to high-level troposphere. Therefore, the strong lidar signals from low-level clouds may have more opportunity to be simulated without being attenuated by upper level clouds. The simulated lidar signal difference between the Morrison scheme and the WSM6 scheme are consistent with the differences in the mean cloud

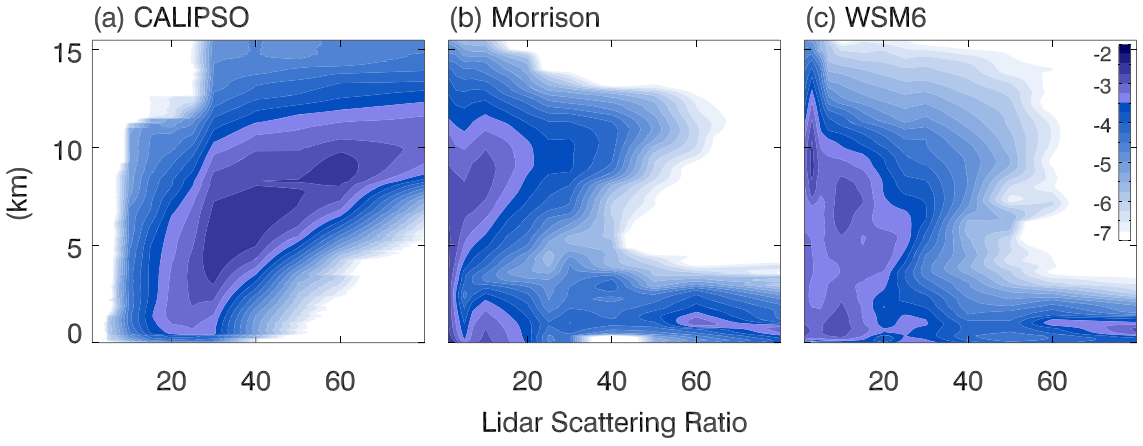

Figure 8. (a) Joint PDF of the CALIPSO lidar scattering ratio and height. Polar WRF simulations with the (b) Morrison scheme and the (c) WSM6 scheme were converted to "satellite-like" lidar scattering radio using the COSP package to obtain the joint PDF. The color scale is the $\log_{10}$ of the joint PDF.

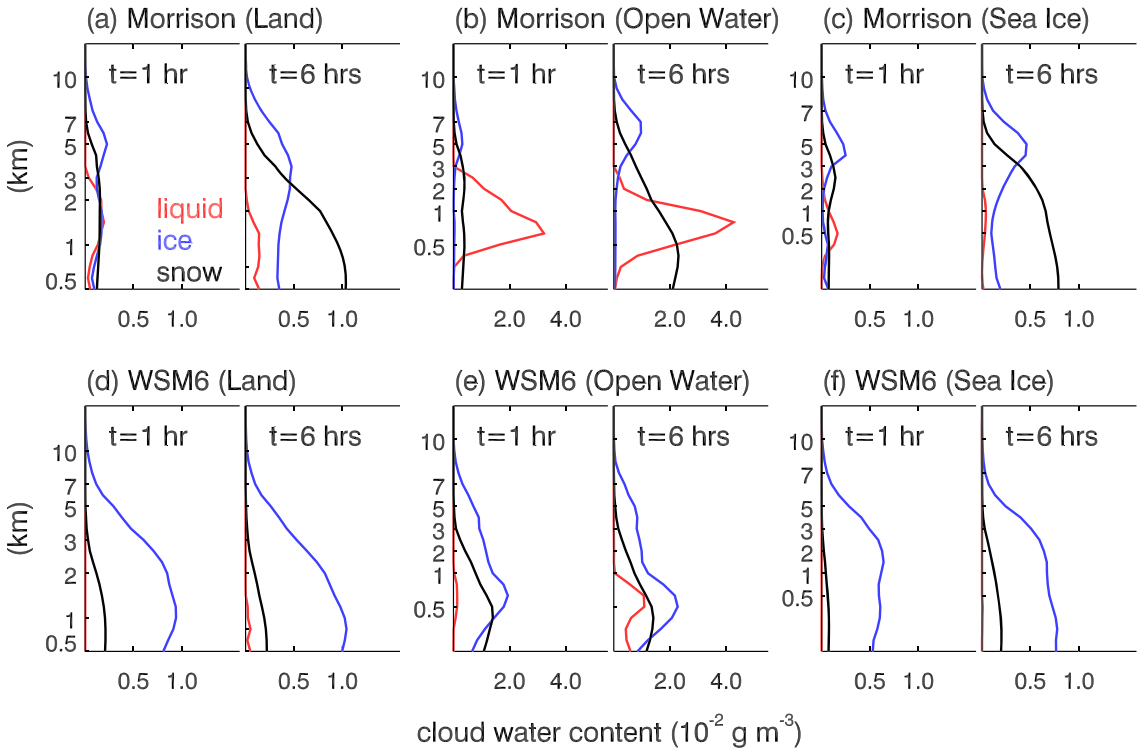

Figure 9. The mean vertical structures of water contents of liquid (red), ice (blue), and snow (black) particles with the (a–c) Morrison scheme and the (d–f) WSM6 scheme at 1 and 6 hr of model integrations initialized at 00 UTC, 24 December 2015. The areas with latitudes higher than 70°N were used, and divided into land surface (a and d), open water (b and e), and sea-ice area (c and f).

amount (Figure 2) and cloud water content (Figure 3). With the Morrison scheme, strong lidar scattering signals above 8 km were more frequently simulated, and the vertical extension of the strong lidar scattering signal near the surface was higher than with the WSM6 scheme.

3.3. Microphysical Processes

In order to examine which microphysical processes are responsible for the differences in the vertical profiles of cloud condensate between the Morrison scheme and the WSM6 scheme, the initial developments of the microphysical properties were investigated. Figure 9 displays the mean vertical profiles of cloud water contents for liquid (red), ice (blue), and snow (black) at 1 and 6 hr after the model was initialized at 00 UTC, 24 December 2015. Because a cloud data assimilation was not used for the initial conditions, all cloud variables are initialized as zero. As the simulation result showed that it took about 4 to 5 hr for the surface precipitation to reach a stable value (not shown), 6 hr was deemed sufficient to examine the outcome of the initial development and short enough to minimize the effects of changing weather conditions. A marked difference between the two schemes is that the Morrison scheme (Figures 9a–9c) shows significant changes in the hydrometeor composition during the initial 6-hr integration, while the WSM6 scheme (Figures 9d–9f) maintains the characteristics of the very early stage with the ice condensate being the dominant category. For the Morrison scheme, liquid clouds quickly developed below about 3 km and continued to build up over open ocean areas (Figure 9b) but diminished with time over sea-ice areas (Figure 9c). While ice condensates show small increases (blue lines in Figures 9a–9c), snow condensates increased greatly (black lines in Figures 9a–9c), becoming the dominant category in the lower troposphere. In addition, only over open sea areas (Figure 9e), the WSM6 scheme produced enough liquid-phase clouds in the lower troposphere to have cloud water contents comparable with frozen-phase clouds.

Figure 10 depicts the process rate terms in the cloud microphysics schemes which contribute to the tendency terms of each hydrometeor. The analyses were done with the same simulation set used for Figure 9. With the Morrison scheme (Figures 10a–10c), the shapes of process terms at 1-hr integration are not similar to those at

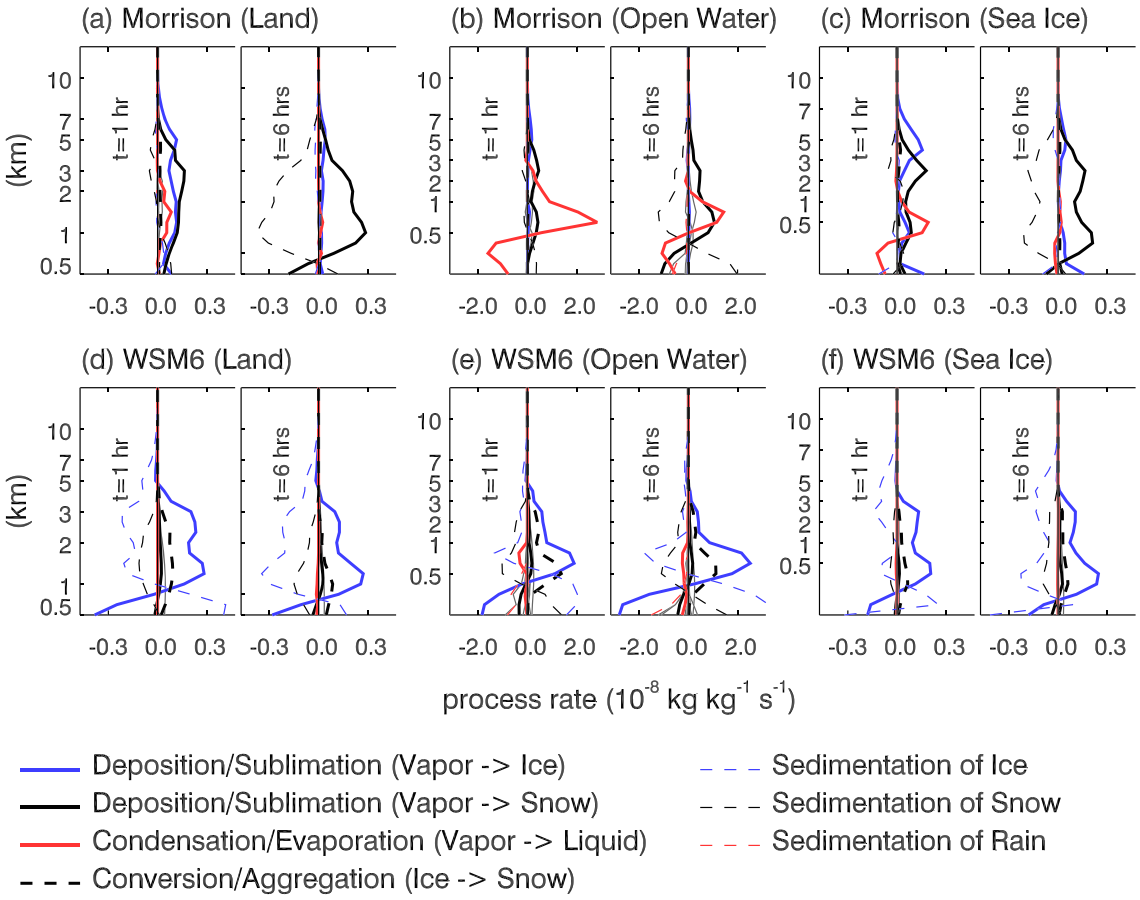

Figure 10. The mean vertical structures of major cloud microphysics process rate terms at 1 and 6 hr of model integrations initialized at 00 UTC, 24 December 2015 when the (a–c) Morrison scheme and the (d–f) WSM6 scheme are used. All the other terms not listed in the legend are plotted in gray lines. The areas with latitudes higher than 70°N were used, and divided into land surface (a and d), open water (b and e), and sea-ice area (c and f).

the 6-hr integration, while the WSM6 scheme (Figures 10d–10f) maintains features of the early stage during the first 6 hr. This is consistent with the vertical profiles of cloud condensate compositions shown in Figure 9. In the mean sense, at the time after 1-hr model integration, the cloud mixing ratio is larger with the WSM6 scheme than that with the Morrison scheme (left sides of Figures 9a–9f). Then, due to the stronger sedimentation of the WSM6 (thin dashed lines in Figures 10d–10f), the cloud mixing ratios become smaller than with the Morrison scheme (right sides of Figures 9a–9f).

The most dominant processes for cloud particle growth were associated with the atmospheric water vapor. Note that the vertical velocity differences are very small between the simulations with the two cloud microphysics schemes (Figure S4). For the Morrison scheme over the land surface and sea ice, the deposition of water vapor by ice/snow particles (thick blue/black lines in Figures 10a and 10c) dominates the process at 6-hr integrations. This explains the abundance of frozen particles in the lower and middle-level troposphere over the regions (blue/black lines in Figures 9a and 9c). As the Morrison scheme shows large liquid water contents at about 1-km height over the open ocean area (red line in Figure 9b), the condensation of water vapor to form liquid clouds shows a strong production rate at the same level (red line in Figure 10b). At levels near the surface, the growth of condensates over land surface and open ocean areas is due mainly to the sedimentations of ice or snow particles (dashed blue/black lines in Figures 10a, 10b, 10d, and 10e), probably originating from upper levels. On the other hand, over the sea ice, the water vapor deposition process is strong even at near-surface levels with the Morrison scheme (thick blue line in Figure 10c), which is not the case for the WSM6 scheme (Figure 10f). The simulations with the WSM6 shows simple vertical structures of cloud water content for all surface types: the ice category dominates in most situations (Figures 9d–9f). They showed a strong deposition process, similar to the Morrison scheme, except that it is the deposition by ice

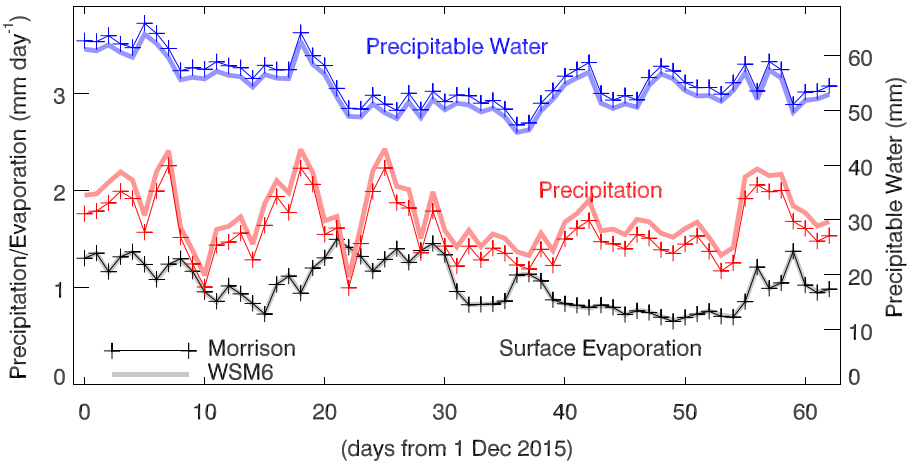

Figure 11. Time series of the daily mean surface evaporation (black), precipitation (red), and precipitable water (blue) from the Polar WRF simulations. The Morrison scheme (marked thin lines) and the WSM6 scheme (thick lines) were used for the cloud microphysics in the simulations. The values were obtained by averaging over the entire simulation domain.

condensate in this case (blue lines in Figures 10d–10f). Another notable feature of the WSM6 scheme is the strong aggregation of ice by snow particles at levels below about 3 km (thick black dashed lines in Figures 10d–10f), while the production of low-level snow particles in the Morrison scheme originates mainly by water vapor depositions or sedimentations from upper levels. Below about 1 to 2 km, sedimentations from upper levels evaporate to influence the atmospheric humidity which, as a result, is slightly (about 1 to 2%) larger with the Morrison scheme (figure not shown). Although small, this might further amplify the differences in the cloud hydrometeor masses between the microphysics schemes even in 48-hr simulations. In addition, at the upper level troposphere over land surface and sea-ice areas, the WSM6 scheme's ice/snow sedimentations were stronger than the deposition processes, which is not the case with the Morrison scheme. The strong sedimentations seem to contribute to the lower cloud top heights with the WSM6 scheme than the Morrison scheme. This may be due to the modified ice process proposed by Hong et al. (2004), which is also implemented in the WSM6 scheme.

3.4. Atmospheric Water Budget

Because the two Polar WRF simulation setups were identical except only for the cloud microphysics scheme, the differences in the outgoing longwave radiation at the TOA (OLR) and the DLR at the surface should be somewhat related to water processes. The water budget within a finite domain is a balance between the water flux at boundaries and surface precipitation once the tendency in the domain can be ignored. Figure 11 shows the time series of the daily mean surface evaporation (black lines), surface precipitation (red lines), and precipitable water in the atmosphere (blue lines) for the Morrison scheme (marked thin lines) and for the WSM6 scheme (thick lines). The values were obtained by averaging over the entire simulation domain. While the surface evaporation, even when the surface temperature is prescribed, can be different between the two schemes due to the differences in the near-surface humidity or wind speed, the difference turned out to be negligible (black lines in Figure 11). On the other hand, the domain-averaged precipitation at the surface (red lines in Figure 11) was significantly stronger with the WSM6 scheme by about 10% of the total precipitation. The blue lines in Figure 11 are the times series of the domain-averaged total precipitable water. It shows a more humid atmosphere with the Morrison scheme than with the WSM6 scheme. This, along with the larger cloud water contents (Figures 3–5), gave rise to a greater atmospheric thermal emissivity with the Morrison scheme than with the WSM6 scheme. Intuitively, the stronger precipitation processes in the WSM6 scheme seem to result in a drier atmosphere and less cloudy sky.

In addition, the surface turbulent latent heat flux was larger with the Morrison scheme than with the WSM6, but by a small amount and only over the ice-free Atlantic Ocean (figure not shown). This is related to the slightly more humid near-surface atmosphere with the WSM6 over the same region when compared to

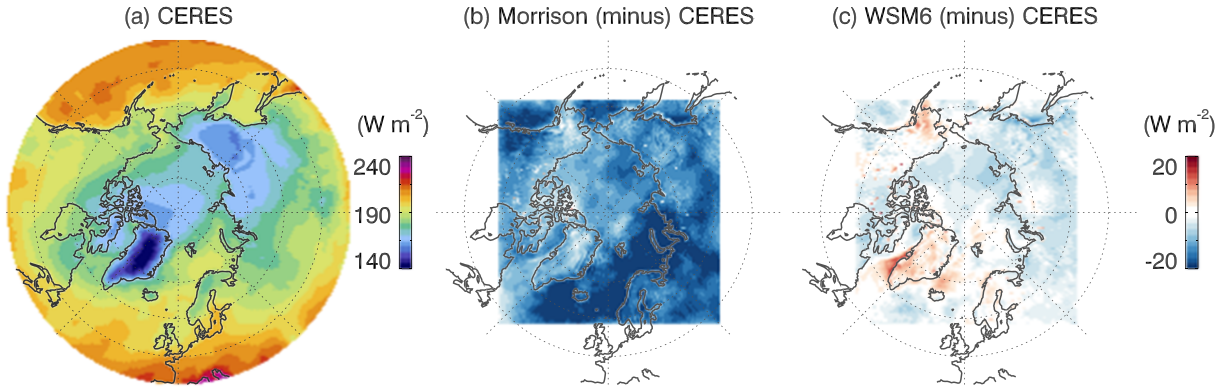

Figure 12. (a) Mean outgoing longwave radiation at the top of atmosphere (OLR) from the CERES observations and the mean differences in the OLR between the Polar WRF simulations and the CERES observation. (b) The Morrison scheme and (c) the WSM6 scheme were used for the cloud microphysics in the simulations.

with the Morrison scheme. The smaller relative humidity from the Morrison scheme may be a result of the warmer near-surface air temperature due to larger surface warming effects from thicker clouds with the Morrison scheme than with the WSM6 scheme. Similarly, the stronger surface warming effect by the thicker clouds from the Morrison scheme resulted in the larger turbulent sensible heat flux from land surface or sea ice than that with the WSM6 scheme. However, over the open-ocean areas, the difference was very small because the sea surface temperature was predefined as a surface boundary condition so it does not respond to forcings.

3.5. Longwave Flux

The cloud influence can be exerted most effectively by changing radiative fluxes at the TOA or the surface, especially during the wintertime over the Arctic region where the effects of convection or precipitation are smaller than any other regions or seasons. Furthermore, the clouds have the largest effect on the temporal and spatial variabilities of OLRs than any other physical element because the surface-to-tropopause lapse rate easily exceeds the equator-to-pole temperature gradient. Figure 12a shows the averaged OLR field of the CERES observations during the two-month period. Within the Polar WRF simulation domain, the Greenland region exhibited the smallest OLR. The Arctic Ocean area that was covered with sea ice and the northern part of East Siberia had OLRs smaller than 180 W m^{-2}. There were sharp contrasts in OLRs across the sea-ice edge north of the Barents-Kara Seas and north of the Chukchi Sea where the warm water intrusions from the Atlantic Ocean and the Pacific Ocean occur.

Figures 12b and 12c indicate the simulated mean OLR bias fields to the CERES observations (Figure 12a) when the Morrison scheme (Figure 12b) and the WSM6 (Figure 12c) was used. With the Morrison scheme, the OLR exhibited a negative bias almost everywhere in the simulation domain that would act to warm the Earth's atmosphere and surface. Since WRF's sea surface temperature is prescribed as an observed value, a larger cloud thickness, a higher cloud top height, and/or a more humid atmosphere than the observations are expected in the simulation with the Morrison scheme. The bias was largest over the open ocean areas of the Atlantic and Pacific Oceans where the surface is warmer and the atmosphere is more humid containing more cloud water. On the other hand, with the WSM6 scheme, the overall OLR bias was significantly reduced than that with the Morrison scheme. Like the simulations with the Morrison scheme, the OLR over the Arctic sea-ice region showed negative bias to observations, but with a smaller magnitude. However, it showed a positive bias over the Atlantic sector of the Arctic Ocean where the Morrison scheme gave rise to a strong negative bias. The region's large OLR difference between the two schemes' simulations is due to the warm surface temperature over the Atlantic open sea that can create large changes in OLRs by relatively small differences in the cloud and/or atmospheric water vapor. The mean difference in OLRs between the two schemes was spatially systematic with about a 10-W m^{-2} weaker thermal outgoing radiation with the Morrison scheme than the WSM6 scheme. This is consistent with the result that the Morrison scheme produced a more humid atmosphere and thicker clouds with higher cloud top than the WSM6 scheme.

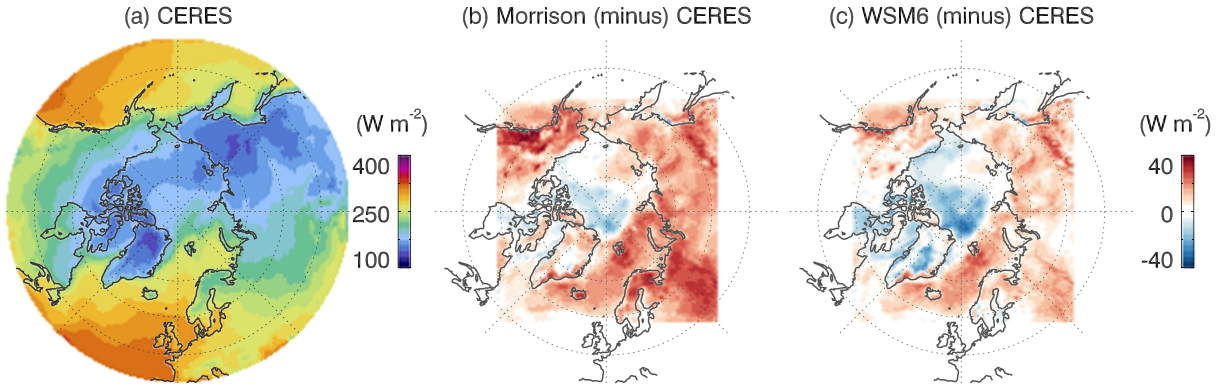

Figure 13. (a) Mean downward longwave radiation (DLR) at the surface from the CERES data set and the mean differences in the DLR between the Polar WRF simulations and the CERES data set. (b) The Morrison scheme and (c) the WSM6 scheme were used for the cloud microphysics in the simulations.

Note that the modeled dynamics fields did not show significant differences between the simulations with the two schemes that might cause the differences in the cloud or radiative flux fields (Figures S1–S3).

In comparison to the OLR, the DLR at the surface is more relevant for the surface weather and climate of the Arctic Ocean and it is directly involved in the cloud radiative effects to the sea-ice variability. Having only the downwelling component, the DLR is determined by the vertical profiles of atmospheric temperature and thermal emissivity which is a strong function of cloud and atmospheric water vapor. Because radiative fluxes at the Earth's surface cannot be measured from satellites, it is typically parameterized using radiative transfer calculations and available information on the atmospheric profiles. The procedure and accuracy of the longwave model in the CERES SSF surface data set are reported in Kratz et al. (2010). Figures 13b and 13c show the mean bias fields to the estimated DLR in the CERES data set (Figure 13a) when the Morrison scheme (Figure 13b) and the WSM6 scheme (Figure 13c) was used. For both the Morrison and the WSM6 schemes, the simulated DLR was stronger than the CERES parameterization in most regions, except for the weaker DLR over the Arctic Ocean areas with large sea-ice concentrations. The positive bias in the DLR over the Atlantic sector of the Arctic Ocean is important, especially over the Barents and Kara Seas. This may act to enhance the surface temperature gradient across the sea-ice edge. As the CERES data set reveals, the mean DLR is large over the open ocean and small over the sea ice, which reflects the different climates of the regions: a warmer and more humid atmosphere with thicker clouds over the open ocean than over the sea ice. This gradient across the sea-ice edge seems to be overestimated in the model simulations

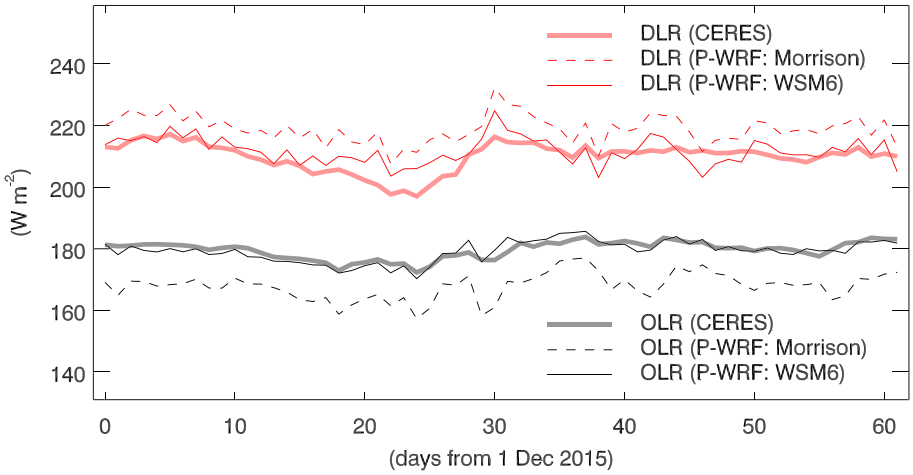

Figure 14. Time series of the daily mean OLR (black) and DLR (red) from the CERES data set (thick solid lines), and the Polar WRF simulations with the Morrison scheme (dashed lines) and the WSM6 scheme (thin solid lines). Only values of the Polar WRF at nadir points of the CERES satellite were used.

Table 2
Correlation Coefficients and Mean Differences (Simulation Minus Satellite Retrieval) in the Outgoing Longwave Radiation at the Top-of-Atmosphere (OLR) and Downward Longwave Radiation at the Surface (DLR) Between the Polar WRF Simulations and the CERES Satellite Data Set

		P-WRF (Morrison)	P-WRF (WSM6)
OLR	Correlation coefficient	0.79	0.87
	Mean difference	-11.7 W m^{-2}	-0.4 W m^{-2}
DLR	Correlation coefficient	0.73	0.67
	Mean difference	9.0 W m^{-2}	1.9 W m^{-2}

Note. The Morrison scheme and the WSM6 were used for the cloud microphysics in the simulations.

with the two cloud microphysics schemes. Note that the mean DLRs were systematically stronger with the Morrison scheme than with the WSM6 scheme everywhere in the simulation domain, but the magnitude of the difference was small over the open ocean but large over the sea ice or land surfaces.

Figure 14 depicts the time series of the daily mean OLR and DLR from the CERES satellite data set and the Polar WRF simulations. It is remarkable that, with the WSM6 scheme, the magnitude and the variation of OLR are very close to the CERES observations with correlation coefficient of 0.87 (Table 2). In comparison, with the Morrison scheme, the day-to-day variation in OLR seems to be a little larger, showing a smaller correlation coefficient ($r = 0.79$) with observations. This suggests an overestimation in the cloud variations with the Morrison scheme. The mean magnitudes of both OLR and DLR from the WSM6 scheme were significantly closer to CERES observations than those from the Morrison scheme (Table 2). It is noted that the mean DLR change was larger than 7 W m^{-2} with only the cloud microphysics scheme switched. Karlsson and Svensson (2013) reported the intermodel spread in the radiative effect of Arctic clouds among current coupled climate models, and during the winter season, the differences in the surface cloud forcing between models did not exceed 20 W m^{-2}. Our results suggest that a significant portion of the climate model uncertainty in simulating the Arctic winter climate could originate from the different cloud representations.

The DLR measurements from ground sites were compared to the simulated DLR (Figure 15). Figure 15 shows the daily mean DLR time series of the observations from the six BSRN sites and of the Polar WRF simulations. Each station's measurement was compared to the time series of the grid where the station is located (Figure 1). Although the BSRN fluxes are direct observations unlike the estimated values of the CERES DLR, their spatial representativeness should be limited to the location of the station. All stations were located near the coast except for the Toravere station. Generally, simulations near coastal regions are expected to be under the strong influence of the sea surface temperature boundary condition. In addition, a strong gradient effect can occur on scales smaller than the grid size, especially at coastlines bordering open seas. With the Morrison scheme, the simulated DLR by the Polar WRF tended to be stronger than observations. However, the mean biases to the ground observations were smaller than those to the CERES estimations. On the other hand, when the WSM6 scheme was used, the DLR values were smaller than the ground observations except at the Lerwick and Barrow stations. This contrasts with the fact that the DLR was consistently larger than the CERES estimation everywhere except over the ice-covered sea surfaces. Nevertheless, consistent with the mean differences in the simulated fields (Figure 13), the DLR values were significantly larger with the Morrison scheme than with the WSM6 scheme at all stations.

Note that four of the six stations are located near the coastline bordering the ice-covered Arctic Ocean across which the mean DLR bias to the CERES estimation changes from positive to negative (Figures 13b and 13c). Therefore, it is challenging to judge the reliability of the estimation by the CERES data set or the representativeness of the ground station observations. However, at the Lerwick station that is surrounded by the open ocean, the DLR values were significantly larger than both the ground observations and the CERES estimations. Considering the strong effect of the sea surface temperature boundary condition at the near-surface level, the bias is likely in part due to an overestimated cloud thickness and the related cloud radiative forcing.

The fact that the OLR was weaker and the DLR was stronger with the Morrison scheme than with the WSM6 scheme over most of the domain implies that the thermal emissivity of the atmosphere is thicker with the Morrison scheme. Not only the larger mixing ratio of clouds (Figure 3) but also the increased amount of liquid-phase particles contribute to the different emissivity between the two schemes' simulations. This results in warming effects on the Earth system by both reducing the outgoing radiation at the TOA and increasing downwelling flux to the surface. The domain-averaged differences in the OLR and the DLR between the two schemes were about –11 and 7 W m^{-2}, respectively, and the magnitudes did not change much throughout the entire simulation period. However, over open ocean areas, while the magnitude of the OLR difference was larger, the magnitude of the DLR difference was smaller than over the sea ice or land surface. Considering that the cloud cover is climatologically larger over open ocean areas than over sea-ice or

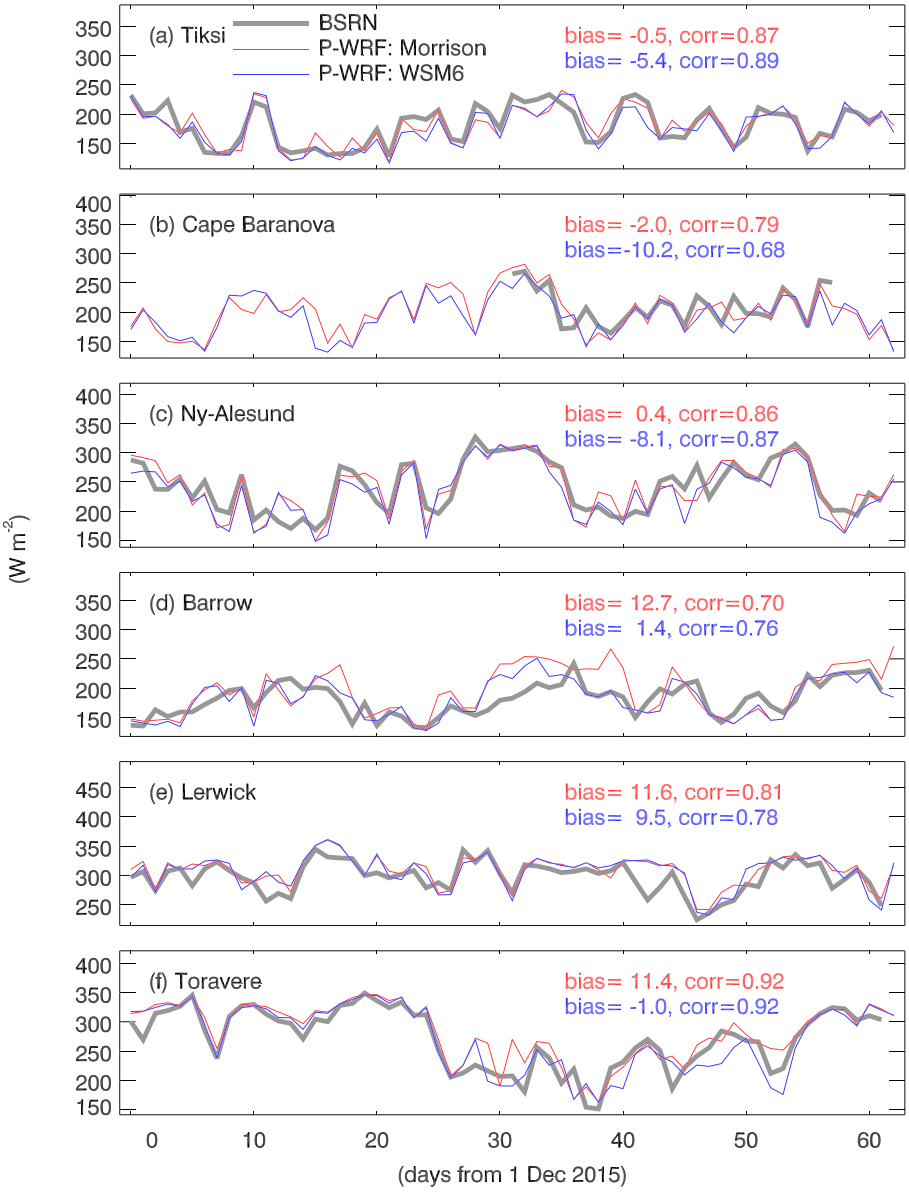

Figure 15. Daily mean time series of the observed DLR (gray) at six BSRN stations: (a) Tiksi, (b) Cape Baranova, (c) Ny-Ålesund, (d) Barrow, (e) Lerwick, and (f) Tõravere and the simulated DLR with the Morrison scheme (red) and the WSM6 scheme (blue) at the grid where each station was located.

land surface areas, the effects of changes in the cloud and/or humidity can be amplified in the OLR and rather muted in the DLR. This is because the OLR responds more sensitively to changes in the clouds over the warm ocean surface. Also, the near-surface air surface temperature which strongly affects the DLR is bound to the prescribed sea surface temperature over open ocean areas, while this not the case over sea-ice or land surface areas.

4. Conclusions

This study investigated whether the performance of the Polar WRF model in simulating Arctic clouds is suitable for further Arctic climate studies, especially for the winter season when the cloud characteristics have not been well understood because of the challenges in obtaining cloud observations. To that end, this study

utilized cloud retrievals from active instruments onboard the CloudSat and CALIPSO satellites. It was shown that clouds in the Polar WRF simulations showed a strong similarity with the physical characteristics of the satellite cloud retrievals. The horizontal and vertical extensions of the clouds were well-captured even for comparisons made on an hourly time scale and a 24-km spatial scale. This included not only the ubiquitous Arctic low-level clouds but also the midtropospheric to upper tropospheric clouds in Arctic wind storms. The vertical profiles of the cloud water contents also were in good agreement with the satellite retrievals with an overestimate near the surface below 1 km where the confidence of the satellite data diminishes.

Two cloud microphysics schemes, the Morrison double moment and the WSM6, were tested. The differences were significant and systematic with the Morrison scheme showing larger cloud amounts and cloud water contents than the WSM6 scheme. This is likely because precipitation is stronger with the WSM6 scheme, thus reducing the precipitable water in the atmosphere compared to the Morrison scheme. This clear difference results in a different longwave radiative flux in the simulations. With the Morrison scheme, the OLR was weaker and the DLR was larger than with the WSM6 scheme. This indicates that the thicker clouds with the Morrison scheme have stronger warming effects than with the WSM6 scheme, both at the TOA by the reduced OLR and at the surface by the increased DLR. It is unclear whether one microphysics scheme is better than the other. The Morrison scheme showed more consistency with observations in simulations of low-level liquid-containing clouds and showed better agreement with the satellite retrievals in the vertical structures of the cloud amount and mixing ratio. On the other hand, both the OLR and DLR values were closer to the CERES observations with the WSM6 scheme. While the two schemes' simulations differ in the hydrometer compositions, the major microphysical processes producing clouds were the deposition of water vapor in both schemes. It is noted that the mean DLR difference between the cloud microphysics was larger than one third of the intermodel spread of the winter cloud radiative effect among the current coupled climate models. The results showed a significant difference in the composition of cloud hydrometeors with varying cloud microphysics schemes. Therefore, further study on the improvement of the modeled cloud physics requires in situ observations of cloud particle shapes, sizes, phases, and amount.

In summary, the Polar WRF successfully reproduced the spatial pattern and the optical properties of winter Arctic clouds. Further, temporal variations of the downward longwave radiation are highly correlated with those from the ground site observations. However, the results indicate that the cloud radiative warming effect is overestimated, and is sensitive to the choice of the cloud microphysics scheme. This should be carefully considered because its impact can be strong enough to alter the underlying sea ice. Nonetheless, as the current study can help estimate amounts of radiative flux errors that are related to the representation of clouds, the Polar WRF can be useful for future studies on Arctic clouds that have remained highly uncertain in coupled climate model simulations.

Acknowledgments
CALIPSO and CERES data were downloaded from https://earthdata.nasa.gov. CloudSat data were obtained from the CloudSat Data Processing Center available at http://www.cloudsat.cira.colostate.edu/data-products. DARDAR cloud retrievals were obtained from the ICARE Data and Services Center available at http://www.icare.univ-lille1.fr/projects/dardar. BSRN observations were retrieved from the PANGAEA Data Publisher which can be accessed via https://bsrn.awi.de/data/data-retrieval-via-pangaea. Final Operational Global Analysis data for the WRF simulation input were downloaded from the NCAR's Research Data Archive available at https://rda.ucar.edu. The NCEP Real-Time Global Sea Surface Temperature data for WRF simulations were downloaded from https://www.nco.ncep.noaa.gov/pmb/products/sst. COSP source code can be obtained from the Cloud Feedback Model Intercomparison Project via https://www.earthsystemcog.org/projects/cfmip/cosp. The namelist files for WRF and COSP simulations can be downloaded from Korea Polar Data Center repository at https://dx.doi.org/doi:10.22663/KOPRI-KPDC-00001341.2. This study was supported by 'Earth System Model-based Korea Polar Prediction System (KPOPS-Earth) Development and Its Application to the High-impact Weather Events originated from the Changing Arctic Ocean and Sea Ice (PE20090)'. Chang-Hoi Ho was supported by the Korea Ministry of Environment (MOE) as 'Climate Change Correspondence Program'. The work of Greg McFarquhar was partially supported by the United States National Science Foundation Grant No. 1762096 and the United States Department of Energy Grant DE-SC0018626. A visit of Chang-Hoi Ho to the University of Oklahoma was funded by School of Meteorology, University of Oklahoma, and Cooperative Institute for Mesoscale Meteorological Studies (CIMMS).

References

Arctic Climate Impact Assessment (2005). *Arctic Climate Impact Assessment: Scientific Report*. New York, NY: Cambridge University Press.

Barton, N. P., & Veron, D. E. (2012). Response of clouds and surface energy fluxes to changes in sea-ice cover over the Laptev Sea (Arctic Ocean). *Climate Research*, *54*, 69–84. https://doi.org/10.3354/cr01101

Bodas-Salcedo, A., Webb, M. J., Bony, S., Chepfer, H., Dufresne, J.-L., Klein, S. A., et al. (2011). COSP: Satellite simulation software for model assessment. *Bulletin of the American Meteorological Society*, *92*(8), 1023–1043. https://doi.org/10.1175/2011bams2856.1

Bryan, G. H., & Morrison, H. (2012). Sensitivity of a simulated squall line to horizontal resolution and parameterization of microphysics. *Monthly Weather Review*, *140*, 202–225. https://doi.org/10.1175/MWR-D-11-00046.1

Cesana, G., Kay, J. E., Chepfer, H., English, J. M., & Boer, G. (2012). Ubiquitous low-level liquid-containing Arctic clouds: New observations and climate model constraints from CALIPSO-GOCCP. *Geophysical Research Letters*, *39*, L20804. https://doi.org/10.1029/2012GL053385

Cess, R. D., Zhang, M. H., Ingram, W. J., Potter, G. L., Alekseev, V., Barker, H. W., et al. (1996). Cloud feedback in atmospheric general circulation models: An update. *Journal of Geophysical Research*, *101*(D8), 12,791–12,794. https://doi.org/10.1029/96JD00822

Chan, M. A., & Comiso, J. C. (2011). Cloud features detected by MODIS but not by CloudSat and CALIOP. *Geophysical Research Letters*, *38*, L24813. https://doi.org/10.1029/2011GL050063

Chan, M. A., & Comiso, J. C. (2013). Arctic cloud characteristics as derived from MODIS, CALIPSO, and CloudSat. *Journal of Climate*, *26*(10), 3285–3306. https://doi.org/10.1175/JCLI-D-12-00204.1

Chepfer, H., Bony, S., Winker, D., Chiriaco, M., Dufresne, J.-L., & Sèze, G. (2008). Use of CALIPSO lidar observations to evaluate the cloudiness simulated by a climate model. *Geophysical Research Letters*, *35*, L15704. https://doi.org/10.1029/2008GL034207

Chernokulsky, A., & Mokhov, I. I. (2012). Climatology of total cloudiness in the Arctic: An intercomparison of observations and reanalyses. *Advances in Meteorology*, *2012*, 542093. https://doi.org/10.1155/2012/542093

Chou, M.-D., Suarez, M. J., Ho, C.-H., Yan, M. M.-H., & Lee, K.-T. (1998). Parameterizations for cloud overlapping and shortwave single-scattering properties for use in general circulation and cloud ensemble models. *Journal of Climate*, *11*, 202–214. https://doi.org/10.1175/1520-0442(1998)011<0202:PFCOAS>2.0.CO;2

Colman, R. (2003). A comparison of climate feedbacks in general circulation models. *Climate Dynamics*, *20*, 865–873. https://doi.org/10.1007/s00382-003-0310-z

Comiso, J. C. (2006). Abrupt decline in the Arctic winter sea ice cover. *Geophysical Research Letters*, *33*, L18504. https://doi.org/10.1029/2006GL027341

Curry, J. A., Schramm, J. L., Rossow, W. B., & Randall, D. (1996). Overview of Arctic cloud and radiation characteristics. *Journal of Climate*, *9*, 1731–1764. https://doi.org/10.1175/1520-0442(1996)009<1731:OOACAR>2.0.CO;2

Delanoë, J., & Hogan, R. J. (2008). A variational scheme for retrieving ice cloud properties from combined radar, lidar, and infrared radiometer. *Journal of Geophysical Research*, *113*, D07204. https://doi.org/10.1029/2007JD009000

Delanoë, J., & Hogan, R. J. (2010). Combined CloudSat-CALIPSO-MODIS retrievals of the properties of ice clouds. *Journal of Geophysical Research*, *115*, D00H29. https://doi.org/10.1029/2009JD012346

Diaz, J. P., González, A., Expósito, F. J., Pérez, J. C., Fernández, J., García-Díez, M., & Taima, D. (2015). WRF multi-physics simulation of clouds in the African region. *Quarterly Journal of the Royal Meteorological Society*, *141*(692), 2737–2749. https://doi.org/10.1002/qj.2560

Driemel, A., Augustine, J., Behrens, K., Colle, S., Cox, C., Cuevas-Agulló, E., et al. (2018). Baseline Surface Radiation Network (BSRN): Structure and data description (1992–2017). *Earth System Science Data*, *10*(3), 1491–1501. https://doi.org/10.5194/essd-10-1491-2018

Francis, J. A., & Hunter, E. (2007). Drivers of declining sea ice in the Arctic winter: A tale of two seas. *Geophysical Research Letters*, *34*, L17503. https://doi.org/10.1029/2007GL030995

Goosse, H., Kay, J. E., Armour, K. C., Bodas-Salcedo, A., Chepfer, H., Docquier, D., et al. (2018). Quantifying climate feedbacks in polar regions. *Nature Communications*, *9*(1), 1919. https://doi.org/10.1038/s41467-018-04173-0

Graversen, R. G., Mauritsen, T., Tjernström, M., Källén, E., & Svensson, G. (2008). Vertical structure of recent Arctic warming. *Nature*, *451*(7174), 53–56. https://doi.org/10.1038/nature06502

Grell, G. A., & Dévényi, D. (2002). A generalized approach to parameterizing convection combining ensemble and data assimilation techniques. *Geophysical Research Letters*, *29*(14), 1693. https://doi.org/10.1029/2002GL015311

Harrison, E. F., Minnis, P., Barkstrom, B. R., Ramanathan, V., Cess, R. D., & Gibson, G. G. (1990). Seasonal variation of cloud radiative forcing derived from the Earth Radiation Budget Experiment. *Journal of Geophysical Research*, *95*(D11), 18,687–18,703. https://doi.org/10.1029/JD095iD11p18687

Haynes, J. M., Marchand, R. T., Luo, Z., Bodas-Salcedo, A., & Stephens, G. L. (2007). A multipurpose radar simulation package: QuickBeam. *Bulletin of the American Meteorological Society*, *88*(11), 1723–1728. https://doi.org/10.1175/BAMS-88-11-1723

Hines, K. M., & Bromwich, D. H. (2017). Simulation of late dummer Arctic clouds during ASCOS with Polar WRF. *Monthly Weather Review*, *145*, 521–541. https://doi.org/10.1175/MWR-D-16-0079.1

Hong, S.-Y., Dudhia, J., & Chen, S.-H. (2004). A revised approach to ice microphysical processes for the bulk parameterization of clouds and precipitation. *Monthly Weather Review*, *132*, 103–120. https://doi.org/10.1175/1520-0493(2004)132<0103:ARATIM>2.0.CO;2

Hong, S.-Y., & Lim, J.-O. J. (2006). The WRF single-moment 6-class microphysics scheme (WSM6). *Journal of the Korean Meteorological Society*, *42*(2), 129–151.

Intergovernmental Panel on Climate Change (2013). Evaluation of climate models. In T. F. Stocker, et al. (Eds.), *Climate Change 2013: The Physical Science Basis. Contribution of Working Group I to the Fifth Assessment Report of the Intergovernmental Panel on Climate Change* (pp. 741–866). Cambridge, UK, & New York, NY: Cambridge University Press. https://doi.org/10.1017/CBO9781107415324.020

Janjić, Z. I. (1994). The step-mountain eta coordinate model: Further developments of the convection, viscous sublayer, and turbulence closure schemes. *Monthly Weather Review*, *122*(5), 927–945. https://doi.org/10.1175/1520-0493(1994)122<0927:TSMECM>2.0.CO;2

Jun, S.-Y., Ho, C.-H., Jeong, J.-H., Choi, Y.-S., & Kim, B.-M. (2016). Recent changes in winter Arctic clouds and their relationships with sea ice and atmospheric conditions. *Tellus A: Dynamic Meteorology and Oceanography*, *68*, 29130. https://doi.org/10.3402/tellusa.v68.29130

Jung, T., Gulev, S. K., Rudeva, I., & Soloviov, V. (2006). Sensitivity of extratropical cyclone characteristics to horizontal resolution in the ECMWF model. *Quarterly Journal of the Royal Meteorological Society*, *132*, 1839–1857. https://doi.org/10.1256/qj.05.212

Karlsson, J., & Svensson, G. (2011). The simulation of Arctic clouds and their influence on the winter surface temperature in present-day climate in the CMIP3 multi-model dataset. *Climate Dynamics*, *36*(3-4), 623–635. https://doi.org/10.1007/s00382-010-0758-6

Karlsson, J., & Svensson, G. (2013). Consequences of poor representation of Arctic sea-ice albedo and cloud-radiation interactions in the CMIP5 model ensemble. *Geophysical Research Letters*, *40*, 4374–4379. https://doi.org/10.1002/grl.50768

Kay, J. E., L'Ecuyer, T., Chepfer, H., Loeb, N., Morrison, A., & Cesana, G. (2016). Recent advances in Arctic cloud and climate research. *Current Climate Change Reports*, *2*(4), 159–169. https://doi.org/10.1007/s40641-016-0051-9

Kim, B.-M., Hong, J.-Y., Jun, S.-Y., Zhang, X., Kwon, H., Kim, S.-J., et al. (2017). Major cause of unprecedented Arctic warming in January 2016: Critical role of an Atlantic windstorm. *Scientific Reports*, *7*(1), 1–9. https://doi.org/10.1038/srep40051

Kim, B.-M., Son, S.-W., Min, S.-K., Jeong, J.-H., Kim, S.-J., Zhang, X., et al. (2014). Weakening of the stratospheric polar vortex by Arctic sea-ice loss. *Nature Communications*, *5*(1), 4646. https://doi.org/10.1038/ncomms5646

Klaus, D., Dethloff, K., Dorn, W., Rinke, A., & Wu, D. L. (2016). New insight of Arctic cloud parameterization from regional climate model simulations, satellite-based, and drifting station data. *Geophysical Research Letters*, *43*, 5450–5459. https://doi.org/10.1002/2015GL067530

Kratz, D. P., Gupta, S. K., Wilber, A. C., & Sothcott, V. E. (2010). Validation of the CERES Edition 2B surface-only flux algorithms. *Journal of Applied Meteorology and Climatology*, *49*, 164–180. https://doi.org/10.1175/2009JAMC2246.1

Kug, J.-S., Jeong, J.-H., Jang, Y.-S., Kim, B.-M., Folland, C. K., Min, S.-K., & Son, S.-W. (2015). Two distinct influences of Arctic warming on cold winters over North America and East Asia. *Nature Geoscience*, *8*, 759–762. https://doi.org/10.1038/ngeo2517

Liou, K. N. (2002). *An Introduction to Atmospheric Radiation*, (2nd ed.). New York, NY: Elsevier.

Listowski, C., & Lachlan-Cope, T. (2017). The microphysics of clouds over the Antarctic Peninsula: Part 2—Modelling aspects within Polar WRF. *Atmospheric Chemistry and Physics*, *17*(17), 10,195–10,221. https://doi.org/10.5194/acp-17-10195-2017

Liu, Y., Key, J. R., Ackerman, S. a., Mace, G. G., & Zhang, Q. (2012). Arctic cloud macrophysical characteristics from CloudSat and CALIPSO. *Remote Sensing of Environment*, *124*, 159–173. https://doi.org/10.1016/j.rse.2012.05.006

Liu, Y., Key, J. R., Francis, J. A., & Wang, X. (2007). Possible causes of decreasing cloud cover in the Arctic winter, 1982–2000. *Geophysical Research Letters*, *34*, L14705. https://doi.org/10.1029/2007GL030042

McCarthy, M., Spillane, S., Walsh, S., & Kendon, M. (2016). The meteorology of the exceptional winter of 2015/2016 across the UK and Ireland. *Weather*, *71*(12), 305–313. https://doi.org/10.1002/wea.2823

McFarquhar, G. M., Zhang, G., Poellot, M. R., Kok, G. L., McCoy, R., Tooman, T., et al. (2007). Ice properties of single-layer stratocumulus during the Mixed-Phase Arctic Cloud Experiment: 1. Observations. *Journal of Geophysical Research*, *112*, D24201. https://doi.org/10.1029/2007JD008633

Mlawer, E. J., Taubman, S. J., Brown, P. D., Iacono, M. J., & Clough, S. A. (1997). Radiative transfer for inhomogeneous atmospheres: RRTM, a validated correlated-k model for the longwave. *Journal of Geophysical Research*, *102*(D14), 16,663–16,682. https://doi.org/10.1029/97JD00237

Morrison, H., Curry, J. A., & Khvorostyanov, V. I. (2005). A new double-moment microphysics parameterization for application in cloud and climate models. Part I: Description. *Journal of the Atmospheric Sciences*, *62*, 1665–1677. https://doi.org/10.1175/JAS3446.1

Morrison, H., Shupe, M. D., & Curry, J. A. (2003). Modeling clouds observed at SHEBA using a bulk microphysics parameterization implemented into a single-column model. *Journal of Geophysical Research*, *108*(D8), 4255. https://doi.org/10.1029/2002JD002229

NCEP (2000). NCEP FNL Operational model global tropospheric analyses, continuing from July 1999. Research Data Archive at the National Center for Atmospheric Research, Computational and Information Systems Laboratory, Boulder, CO, https://doi.org/10.5065/D6M043C6

Oreopoulos, L., Cho, N., & Lee, D. (2017). New insights about cloud vertical structure from CloudSat and CALIPSO observations. *Journal of Geophysical Research: Atmospheres*, *122*(17), 9280–9300. https://doi.org/10.1002/2017JD026629

Overland, J. E., Dethloff, K., Francis, J. A., Hall, R. J., Hanna, E., Kim, S.-J., et al. (2016). Nonlinear response of mid-latitude weather to the changing Arctic. *Nature Climate Change*, *6*(11), 992–999. https://doi.org/10.1038/nclimate3121

Park, D.-S. R., Lee, S., & Feldstein, S. B. (2015). Attribution of the recent winter sea ice decline over the Atlantic sector of the Arctic Ocean. *Journal of Climate*, *28*, 4027–4033. https://doi.org/10.1175/JCLI-D-15-0042.1

Pinto, J. O. (1998). Autumnal mixed-phase cloudy boundary layers in the Arctic. *Journal of the Atmospheric Sciences*, *55*, 2016–2038. https://doi.org/10.1175/1520-0469(1998)055<2016:AMPCBL>2.0.CO;2

Pope, V. D., & Stratton, R. A. (2002). The processes governing horizontal resolution sensitivity in a climate model. *Climate Dynamics*, *19*, 211–236. https://doi.org/10.1007/s00382-001-0222-8

Shupe, M. D. (2011). Clouds at arctic atmospheric observatories. Part II: Thermodynamic phase characteristics. *Journal of Applied Meteorology and Climatology*, *50*(3), 645–661. https://doi.org/10.1175/2010jamc2468.1

Shupe, M. D., Matrosov, S. Y., & Uttal, T. (2006). Arctic mixed-phase cloud properties derived from surface-based sensors at SHEBA. *Journal of the Atmospheric Sciences*, *63*, 697–711. https://doi.org/10.1175/JAS3659.1

Skamarock, W. C., Klemp, J. B., Dudhia, J., Gill, D. O., Barker, D. M., Duda, M. G., et al. (2008). A description of the Advanced Research WRF version 3. In *NCAR Technical Note* (NCAR/TN-4751STR, pp. 113). https://doi.org/10.5065/D68S4MVH

Soden, B. J., & Held, I. M. (2006). An assessment of climate feedbacks in coupled ocean–atmosphere models. *Journal of Climate*, *19*, 3354–3360. https://doi.org/10.1175/JCLI3799.1

Stephens, G. L., Vane, D. G., Boain, R. J., Mace, G. G., Sassen, K., Wang, Z., et al., & the CloudSat Science Team (2002). The CloudSatmisson and the A-Train: A new dimension of space-based observations of clouds and precipitation. *Bulletin of the American Meteorological Society*, *83*(12), 1771–1790. https://doi.org/10.1175/BAMS-83-12-1771

Tewari, M., Chen, F., Wang, W., Dudhia, J., LeMone, M. A., Mitchell, K., et al. (2004). Implementation and verification of the unified Noah land-surface model in the WRF model. Paper presented in 20th Conference on Weather Analysis and Forecasting/16th Conference on Numerical Weather Prediction, American Meteorological Society, Seattle, WA.

Thiébaux, J., Rogers, E., Wang, W., & Katz, B. (2003). A new high-resolution blended real-time global sea surface temperature analysis. *Bulletin of the American Meteorological Society*, *84*(5), 645–656. https://doi.org/10.1175/BAMS-84-5-645

Van Weverberg, K., Vogelmann, A. M., Lin, W., Luke, E. P., Cialella, A., Minnis, P., et al. (2013). The role of cloud microphysics parameterization in the simulation of mesoscale convective system clouds and precipitation in the tropical western Pacific. *Journal of the Atmospheric Sciences*, *70*(4), 1104–1128. https://doi.org/10.1175/JAS-D-12-0104.1

Webb, M. J., Senior, C. A., Sexton, D. M. H., Ingram, W. J., Williams, K. D., Ringer, M. A., et al. (2006). On the contribution of local feedback mechanisms to the range of climate sensitivity in two GCM ensembles. *Climate Dynamics*, *27*(1), 17–38. https://doi.org/10.1007/s00382-006-0111-2

Wielicki, B. A., Barkstrom, B. R., Harrison, E. F., Lee, R. B., Louis Smith, G., & Cooper, J. E. (1996). Clouds and the Earth's Radiant Energy System (CERES): An Earth Observing System experiment. *Bulletin of the American Meteorological Society*, *77*, 853–868. https://doi.org/10.1175/1520-0477(1996)077<0853:CATERE>2.0.CO;2

Wilson, A. B., Bromwich, D. H., & Hines, K. M. (2012). Evaluation of Polar WRF forecasts on the Arctic System Reanalysis domain: 2. Atmospheric hydrologic cycle. *Journal of Geophysical Research*, *117*, D04107. https://doi.org/10.1029/2011JD016765

Winker, D. M., Vaughan, M. A., Omar, A., Hu, Y., Powell, K. A., Liu, Z., et al. (2009). Overview of the CALIPSO mission and CALIOP data processing algorithms. *Journal of Atmospheric and Oceanic Technology*, *26*(11), 2310–2323. https://doi.org/10.1175/2009JTECHA1281.1